https://doi.org/10.5194/essd-2026-411
Preprint. Discussion started: 28 July 2026

Arctic aerosol and meteorological observations using airborne and ground-based systems in spring 2024

Malte Schuchard[1], Konrad Bärfuss[1], Lutz Bretschneider[1], Thomas Conrath[2], Andreas Held[3], Ralf Käthner[2], Mona Kellermann[2], Astrid Lampert[1], Theresa Mathes[3], Joshua Müller[4], Christian Pilz[2], Andreas Schlerf[1], Holger Siebert[2], Birgit Wehner[2], and Barbara Harm-Altstädter[1]

[1]Institute of Flight Guidance, Technische Universität Braunschweig, Braunschweig, Germany
[2]Atmospheric Microphysics Department, Leibniz Institute for Tropospheric Research, Leipzig, Germany
[3]Chair of Environmental Chemistry and Air Research, Technische Universität Berlin, Berlin, Germany
[4]Leipzig Institute for Meteorology, University of Leipzig, Leipzig, Germany

Correspondence: Malte Schuchard (malte.schuchard@tu-braunschweig.de)

Abstract. A comprehensive observational data set of the vertical and horizontal distribution of aerosol particles and meteorological parameters is presented. Data were obtained from an Arctic field campaign conducted with three different measurement platforms deployed at distinct locations in Ny-Ålesund, Svalbard, during the transition period from spring to summer between 19 May 2024 and 8 June 2024. The uncrewed aerial system ALADINA was used for vertical and horizontal profiling in the lowermost 930 m above sea level, covering 38 measurement flights including 143 vertical profiles and 62 horizontal flight legs at different constant altitudes. The tethered balloon system BELUGA performed 90 vertical profiles up to a maximum altitude of 1.3 km above sea level. Together, the airborne platforms provide information on particle number concentrations, including ultrafine particles with diameters below 20 nm, size distribution from the nucleation to coarse mode, and meteorological parameters (i.e. temperature, humidity, pressure, wind direction, wind speed, and short-wave irradiance). In addition, a surface flux gradient system was applied for the calculation of turbulent fluxes of sensible heat and vertical motion of particles, covering a sampling time of about 214 h. An illustrative case study is shown for 3 June 2024, highlighting the spatial variability of aerosol particles, which is strongly influenced by the stability of the polar atmospheric boundary layer. The high-resolution observations enable the study of processes of aerosol–cloud interactions, new particle formation and lead to a generally improved understanding of the spatial distribution of Arctic aerosols. The data of all three measurement platforms are publicly available on the world data centre PANGAEA as described in the data availability section.

1 Introduction

The Arctic environment is rapidly changing as a result of the phenomenon called Arctic amplification (AA), which causes an increase in surface temperature that is about four times higher than the global average (Rantanen et al., 2022). This effect is caused by several feedback mechanisms involving the atmosphere, land surfaces, ocean and sea ice, and have led to fast changes in polar regions, especially in recent years (Goosse et al., 2018; Wendisch et al., 2023). These substantial changes are primarily driven by the anthropogenic impact on the Earth's climate system, dominated by a significant and ongoing growth

https://doi.org/10.5194/essd-2026-411
Preprint. Discussion started: 28 July 2026

Open Access Earth System Science Data Discussions

in emissions of greenhouse gases, leading to the most visible consequence in the form of sea ice loss in the central Arctic (Dai et al., 2019; Kim et al., 2023). The decrease in sea ice surface cover implies various changes in the interaction between surface, ocean, and atmosphere, manifested as changes in the Earth's radiation budget (e.g., Huang et al., 2021; Pithan and Mauritsen, 2014), cloud properties (Shupe and Intrieri, 2004), vertical transport of water, temperature and impulse (Chung and Feldl, 2024), bio-geochemical processes (Vancoppenolle et al., 2013; Zitoun et al., 2024), as well as aerosol particles (e.g., Browse et al., 2014; Dall´Osto et al., 2017; Pernov et al., 2022; Wang et al., 2018). The role of aerosol particles remains uncertain, as current knowledge of their sources and interactions with the Arctic atmosphere during their lifetime is limited (Schmale et al., 2021), as the processes are highly complex and inhomogeneous in space and time. There are several contributing factors to this phenomenon, some of which can influence each other. For instance, aerosol particles strongly affect the Earth's surface energy balance through two main different mechanisms. Firstly, the direct effect refers to the scattering and absorption of solar radiation by aerosol particles based on their optical properties, which are characterised by their size, chemical and physical composition as well as their mixing state (Charlson et al., 1991). Secondly, the indirect effect relates to aerosol-cloud interactions (ACI), including aerosol particles acting as cloud condensation nuclei (CCN) or ice nuclei (IN), which influences the formation and characteristics of clouds (Albrecht, 1989; Twomey, 1977). In the high Arctic, the aerosol particle number concentration (N) and CCN concentration are generally low. Especially during summer, clouds cannot always form under supersaturated water vapour conditions due to the low aerosol concentration (Duplessis et al., 2024). Consequently, minor changes in the already low concentration of N from anthropogenic or natural sources can significantly impact cloud properties (Mauritsen et al., 2011). However, fog events have been observed in the Arctic during late summer that persisted for several hours at particle number concentrations less than 10 cm^{-3} (Duplessis et al., 2024). Regarding the Earth's climate and the AA, Arctic clouds can either lead to effects that warm or cool surface temperatures. Their influence depends on the characteristics relating to ACI, but also on seasonal conditions and surface properties (Wendisch et al., 2023). For instance, a two-year study from Ny-Ålesund showed a cooling effect of clouds in summer and a warming effect from September to April/May with an annual positive cloud radiative forcing (Ebell et al., 2020).

In general, there are two main seasonal patterns of aerosol size distribution in the Arctic. During winter and spring, N is dominated by accumulation mode particles. In summer, aerosols are dominated by nucleation and Aitken mode particles, which are predominantly formed locally (e.g., Dall'Osto et al., 2020; Tunved et al., 2013). Previous studies proposed various possible origins for Arctic aerosol particles across different spatial scales. These include marine and continental sources that are advected over long distances by atmospheric transport (e.g., Leck et al., 2002; Stohl, 2006), entrainment from the free troposphere aloft (e.g., Igel et al., 2017; Price et al., 2023), and local processes or sources including blowing snow (e.g., Frey et al., 2020), sea ice melt (e.g., Dall´Osto et al., 2017, 2018), primary marine aerosol emissions from biologically active open water (e.g., Orellana et al., 2011), and secondary aerosol formation from biogenic volatile organic compounds (e.g., Beck et al., 2021; Mungall et al., 2017). However, assessing the actual role of aerosol particles becomes even more challenging when dynamic processes are considered in the atmosphere. Atmospheric dynamics have a significant influence on the spatial distribution of aerosol particles, which often exhibits high temporal variability (e.g., Chen et al., 2021). To date, the majority of field studies have been based on fixed-point, surface-based observatories, including instrumentation installed on vessels

https://doi.org/10.5194/essd-2026-411
Preprint. Discussion started: 28 July 2026

Open Access Earth System Science Data Discussions

navigating through the Arctic ocean. To investigate the spatial distribution of aerosol properties, aircraft-based observations are, in principle, indispensable and have been conducted extensively in the Arctic. Research aircraft can be equipped with the necessary instrumentation and, due to their flight times of several hours, can cover large areas, thereby yielding statistically significant results. However, there are limitations where other observational approaches may be advantageous. In areas with highly complex topography and at very low altitudes, measurements using crewed aircraft are limited in the Arctic for safety reasons. Therefore, to achieve a profound understanding of aerosol processes in the atmospheric boundary layer (ABL) and to improve atmospheric models in the Arctic, high quality data with high spatial and temporal resolution are required (e.g., Matsui and Liu, 2022). This gap can be excellently filled by a combination of uncrewed aerial systems (UAS) and tethered balloons, in parallel to long-term observations on the ground. These observations contribute to a more profound understanding of the small-scale distribution and effects of NPF, CCN, and ACI, as well as particle growth processes, mixing, and horizontal transport of aerosol particles between the surface and the lower part of the atmosphere for different ABL stability conditions.

This publication presents an extensive approach combining different observational platforms in a joint field campaign. Three different measurement systems were deployed at the coastal Arctic site in Ny-Ålesund (Spitsbergen, Norway) during the transition period from spring to summer between 19 May 2024 and 8 June 2024. To study the horizontal and vertical distribution of aerosol particles and interactions with meteorological parameters, the UAS ALADINA (Altstädter et al., 2015), developed by Technische Universität Braunschweig, and the tethered balloon system BELUGA (Egerer et al., 2019), developed by the Leibniz Institute for Tropospheric Research (TROPOS), were deployed up to an altitude of 1.3 km. To quantify the turbulent vertical transport of aerosol particles, a surface flux gradient system (Mathes et al., 2025a) was deployed close to the launch point of BELUGA at ground level. The observations of the field campaign consist of aerosol properties (N of ultrafine aerosol particles (UFPs) with diameters less than 20 nm, size distributions from the nucleation to coarse mode, near-surface particle fluxes), meteorology (temperature, humidity, pressure, wind, irradiance), as well as surface conditions (surface temperature).

Herein, this article is structured as follows: Sect. 2 provides an overview of the field campaign in Ny-Ålesund, including an introduction to the measurement site in Sect. 2.1, and information on the observation period and data availability of the individual systems in Sect. 2.2. The three different measurement systems, including instrumentation and data post-processing, are presented in Sect. 3. As an illustrative example, the measurements obtained on 3 June 2024 are presented in Sect. 4. This exemplary case study of the spatial distribution and variability of aerosol particles highlights the potential of this combined measurement approach and serves to advance high-precision ABL parameters and aerosol observations. Finally, Sect. 5 provides a conclusion and the availability of the individual data sets of the three measurement systems is described in Sect. 6.

2 Overview of field campaign

2.1 Research area

The research village Ny-Ålesund (78.92° N, 11.93° E; 11 m above sea level (a.s.l.)) and its surroundings are characterised by a highly heterogeneous terrain (see Fig. 1a,b), combining tundra, hills, and mountains reaching around 700 m a.s.l., as well as glaciers, fjords, and the adjacent Arctic ocean. Pronounced changes in surface conditions appear over small distances of about

https://doi.org/10.5194/essd-2026-411
Preprint. Discussion started: 28 July 2026

a few hundred meters, including snow consisting of different altering stages, ice, soil and open water. The surface wind field is mainly influenced by an orographic channelling effect along the Kongsfjord, resulting in two primary wind regimes that are oriented in the northwest and southeast wind direction (Beine et al., 2001). The prevailing wind directions are combined with multiple local wind regimes, induced by the complex orography that further causes a strong rotation in the wind field above the altitude of 500 m a.s.l. (Graßl et al., 2022; Schön et al., 2022).

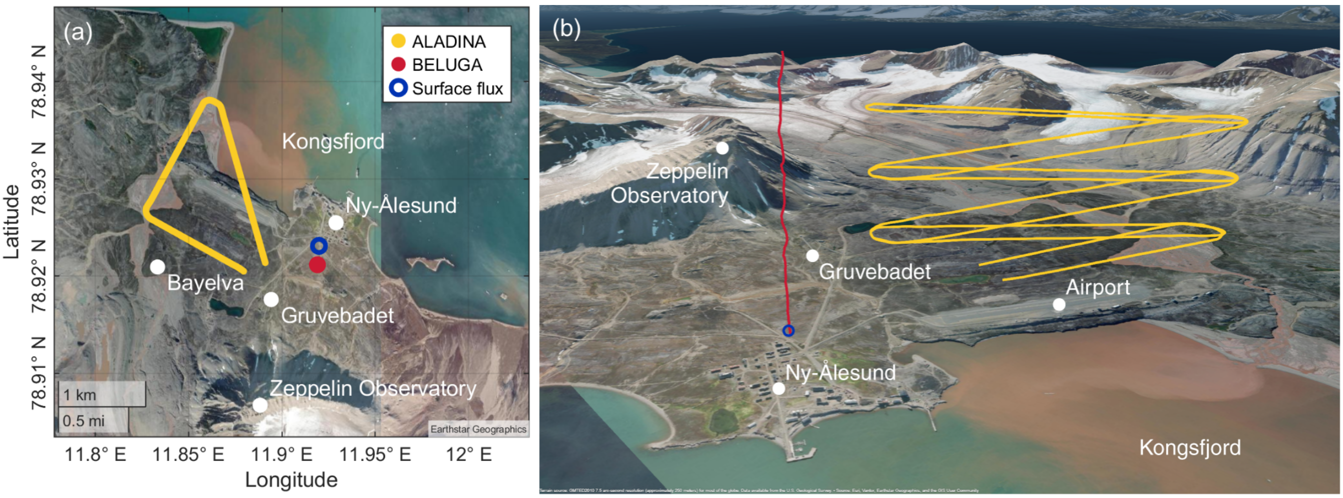

Figure 1. Map of the Ny-Ålesund research area shown as a bird's-eye view (a) and side view (b). The figures display the measurement locations of the three different systems used in this study to investigate aerosol and meteorological properties: exemplary horizontal (a) and vertical (b) flight paths of ALADINA (yellow line), a representative BELUGA flight path (red) and the location of the surface flux gradient system (blue circle) at ground level. Ground-based stations (white dots) include the Zeppelin Observatory, Gruvebadet Atmosphere Laboratory, the Bayelva research site and the AWIPEV Research Base in Ny-Ålesund. Map data sources: (a) Earthstar Geographics. (b) GMTED2010 7.5 arc-second resolution (approximately 250 meters) for most of the globe, data available from the U.S. Geological Survey; Esri, Vantor, Earthstar Geographics, and the GIS User Community | Powered by Esri.

The investigation area has a profound history of observatory measurements, covering a multitude of parameters including aerosol properties, chemistry and meteorological parameters. The measurement infrastructure is distributed across various ground-based stations in Ny-Ålesund and its surrounding area, such as the Zeppelin Observatory (e.g., Platt et al., 2022), which is located on Zeppelin Mountain at 472 m a.s.l. (see Fig. 1a,b). Other ground-based stations include the Gruvebadet Atmosphere Laboratory (e.g., Lupi et al., 2016), which is located southwest of Ny-Ålesund at 50 m a.s.l. (see Fig. 1a,b), the Bayelva research site, situated 3 km west from Ny-Ålesund (e.g., Boike et al., 2018), and the French-German AWIPEV (**A**lfred-**W**egener-**I**nstitut; **I**nstitut polaire français **P**aul-**É**mile **V**ictor) Research Base in Ny-Ålesund (e.g., Maturilli et al., 2013).

2.2 Research strategy and period

The research strategy for the field campaign comprises two main elements. First, the two airborne systems ALADINA and BELUGA are used simultaneously whenever feasible in operation to study the vertical and horizontal distributions of aerosol particles in interaction with meteorological parameters and different ABL stability conditions. Second, continuous ground-based measurements are obtained with the surface flux gradient system to quantify the vertical turbulent transport of aerosol particles.

Measurements with the fixed-wing UAS ALADINA (see Sect. 3.1) focus on aerosol properties and meteorological parameters in the vertical distribution from the surface to a maximum altitude of 930 m a.s.l. and in the horizontal distribution within an operation area of approximately 1.5 km^2. Therefore, ALADINA was operated in two different flight patterns. First, horizontal patterns consisted of straight and level legs flown parallel and perpendicular to the two primary wind regimes (northwest and southeast direction) at several fixed altitudes (see Fig. 1a). Second, vertical profiles were performed as steady ascents or descents, interrupted by level 180° turns (see Fig. 1b). A vertical profile up to the maximum altitude typically requires about 7 min per ascent or descent, while a horizontal pattern lasts for approximately 3 min at each constant altitude. The daily measurement strategy depended on weather conditions and available operation time, as research flights were not possible during temporary air traffic that connects Ny-Ålesund and Longyearbyen. Both flight patterns were repeated during multiple daily ALADINA flights of approximately 40 min, with typical turnaround times of about 20 min. If possible, several vertical profiles up to the maximum altitude were combined with horizontal legs at a minimum of three different altitudes. However, horizontal legs were not performed during every measurement flight, and the achievable maximum altitude depended on the prevailing cloud base height (CBH), as for safety reasons flight operations are performed out of clouds. The rapid and repeatedly executed vertical profiles provide high temporal resolution of aerosol concentration changes throughout the measurement day, while the horizontal legs capture the spatial heterogeneity and short-term variability of aerosols within the research area. ALADINA was operated from the local airport (see Fig. 1b) between 20 May 2024 and 4 June 2024 on nine measurement days. In total, approximately 20 h of data are available from 38 measurement flights, comprising 143 vertical profiles and 62 horizontal flight legs at multiple constant altitudes, typically at approximately 470 m a.s.l. as well as at altitude levels above and below. The horizontal legs were operated above land and water, including transects that crossed the coastline to the Kongsfjord. Only the two described flight patterns are considered in data post-processing. Other flight segments, such as take-off, landing, and calibration manoeuvres are excluded due to low data quality (see Sect. 3.1.2), thereby reducing the effective flight duration, which is represented in the final data set.

The tethered balloon system BELUGA allows small-scale vertical profiling with interchangeable instruments attached to a tether line. During this field campaign, the balloon was operated with three different payloads to observe meteorological and aerosol microphysical parameters (see Sect. 3.2). The measurement strategy and choice of payload depended on the prevailing meteorological conditions and observed aerosol concentrations. If possible, several vertical profiles with maximum altitudes reaching 1200 m a.s.l. were conducted during each BELUGA flight of up to 3 h duration with a mean ascent and descent rate of 0.5 m s^{-1}. The system was also maintained at selected constant altitudes to extend the sampling time, for example within

https://doi.org/10.5194/essd-2026-411
Preprint. Discussion started: 28 July 2026

Open Access Earth System Science Data Discussions

pronounced aerosol particle layers or at cloud base and cloud top. BELUGA was operated outside of but close to the village of Ny-Ålesund (see Fig. 1a,b), using a temporary ground-based winch and pulley system. On eight days between 19 May 2024 and 7 June 2024, a total of 90 profiles (ascent or descent) were completed during 23 measurement flights, reaching varying
140 maximum altitudes and collecting approximately 39 h of data.

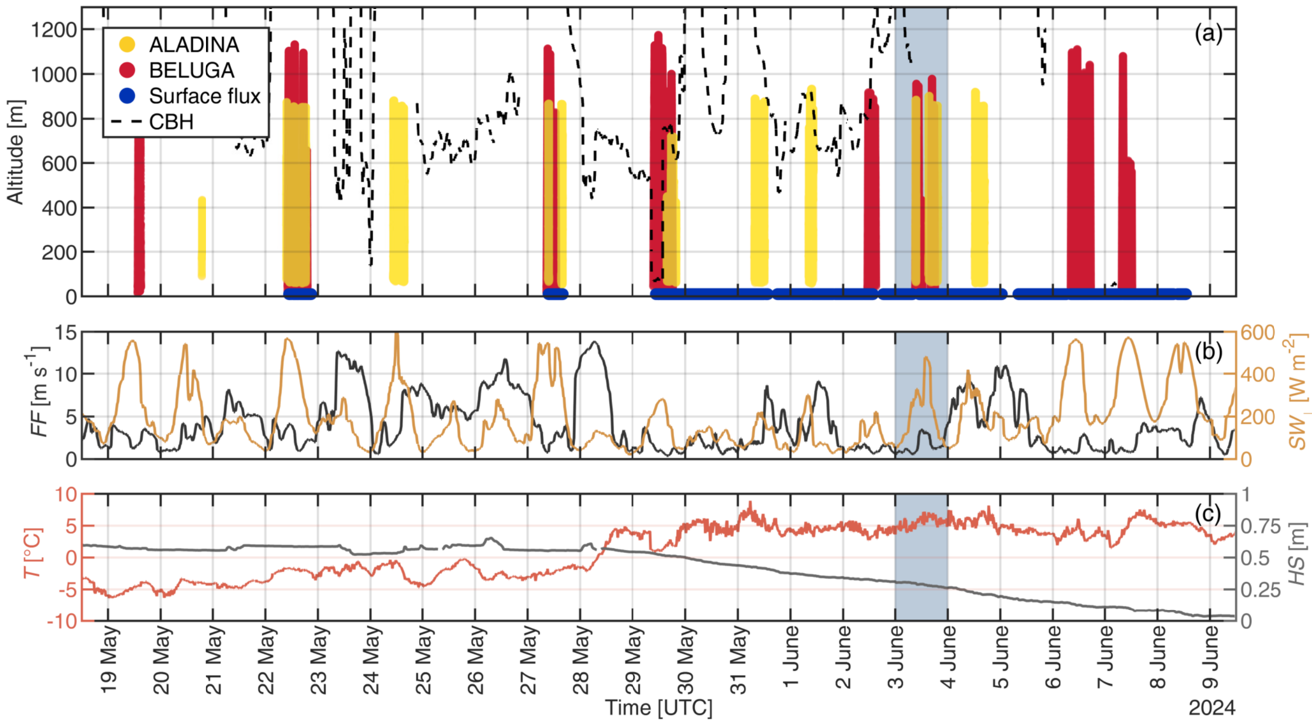

Figure 2. Data availability of the three different measurement systems and time series of selected parameters during the research period in May and June 2024, in 2 h median intervals. The blue background shading indicates the case study on 3 June 2024 (see Sect. 4). (a) Data availability and altitudes a.s.l. of ALADINA (yellow), BELUGA (red) and surface flux gradient system (blue) together with cloud base height (CBH, m, dashed black line). (b) Wind speed (FF, m s^{-1}, black line) at 10 m a.g.l. and short-wave downward irradiance ($SW_{\downarrow}$, W m^{-2}, amber line). (c) Air temperature (T, °C, red line) at 10 m a.g.l. and snow height (HS, m, grey line).

The combined use of ALADINA and BELUGA links high temporal resolution, spatially distributed observations obtained from the UAS with quasi-stationary observations, high vertical resolution profiling derived from the tethered balloon, including in-cloud measurements to observe ACI. In turn, the surface flux gradient system (see Sect. 3.3) provides continuous information on near-surface aerosol particle number concentration, as well as wind speed and temperature profiles from 0.1 m above ground
145 level (a.g.l.) up to a height of 1.34 m a.g.l. The vertical particle flux and sensible heat flux are then calculated based on the measured data. The daily runtime of the measurements varied from 6 h to 23 h, depending on the prevailing meteorological

https://doi.org/10.5194/essd-2026-411
Preprint. Discussion started: 28 July 2026

conditions. The system was operated at a distance of around 50 m from the ground base of BELUGA on 13 days between 22 May 2024 and 8 June 2024, collecting approximately 214 h of data.

Table 1. Daily sampling time (h:min) of the three measurement systems after data post-processing, including the number of vertical profiles (V) and horizontal patterns with constant altitude level (H) for ALADINA and the number of vertical profiles (V) for BELUGA. n/o: not operated.

Date	ALADINA (V, H)	BELUGA (V)	Surface flux
19 May 2024	n/o	1:28 (4)	n/o
20 May 2024	0:05 (2, 0)	n/o	n/o
22 May 2024	3:22 (24, 6)	7:05 (16)	6:40
24 May 2024	2:39 (18, 8)	n/o	n/o
27 May 2024	1:07 (10, 0)	4:27 (8)	5:40
29 May 2024	2:40 (20, 22)	7:44 (12)	14:00
30 May 2024	n/o	n/o	21:40
31 May 2024	2:38 (21, 4)	n/o	17:00
1 June 2024	1:19 (11, 0)	n/o	22:20
2 June 2024	n/o	3:23 (8)	18:20
3 June 2024	**3:14 (21, 9)**	**3:53 (8)**	**20:40**
4 June 2024	2:51 (16, 13)	n/o	21:20
5 June 2024	n/o	n/o	16:20
6 June 2024	n/o	6:49 (18)	19:40
7 June 2024	n/o	4:16 (16)	21:20
8 June 2024	n/o	n/o	8:40
Total	19:55 (143, 62)	39:05 (90)	213:40

Figure 2 provides an overview of the data availability for the three different measurement systems and selected meteorological parameters during the entire research period from 19 May 2024 to 8 June 2024, including cloud base height, wind speed, short-wave downward irradiance and air temperature derived from AWIPEV Research Base (adapted from: Maturilli, 2020a, b, 2022), as well as snow height measured at the Bayelva research site (adapted from: Boike et al., 2018; Boike et al., 2022). The measurements obtained on 3 June 2024 are presented in Sect. 4 as a representative case study. Colour schemes employed in Fig. 2 and in the subsequent figures are based on Crameri (2023). The ALADINA operation is limited by low clouds, fog, precipitation, wind speed and gusts exceeding 15 m s^{-1}, also no icing conditions. BELUGA operation is limited to surface wind speed below 5 m s^{-1}, but was possible during fog and cloud conditions. Additional constraints in flight time resulted from limited working hours outside the boundaries of Ny-Ålesund and from occasionally required maintenance of the airborne systems. Consequently, no airborne data are available on specific days, for example, on 23 May 2024 and from 25 May 2024 to 26 May 2024 due to precipitation, appearance of low clouds and high wind speed above 10 m s^{-1} (see CBH and

https://doi.org/10.5194/essd-2026-411
Preprint. Discussion started: 28 July 2026

wind speed (FF) at 10 m a.g.l. in Fig. 2a,b). A comprehensive overview of data availability is provided in Table 1, including the daily sampling time after data post-processing and the numbers of flight profiles for the two airborne platforms.

The field campaign in Ny-Ålesund was conducted during the transition from spring to summer 2024, coinciding with continuous daylight during the polar day which began on 17 April 2024. In general, this period is characterised by a high frequency of NPF driven by an increase in solar radiation, providing optimal conditions for studying the occurrence of UFPs (Lee et al., 2020). Therefore, the selected research period is suitable to address open questions regarding potential sources of NPF and ACI (Dall´Osto et al., 2018). The short-wave downward irradiance ($SW_{\downarrow}$) frequently exceeded 500 W m^{-2} under clear-sky conditions (see Fig. 2b), thus promoting favourable conditions for photochemical processes. At the beginning of the field campaign, air temperature (T) was below 0°C and snow height (HS) was constant. From 28 May 2024 onwards, the air temperature increased rapidly, resulting in the onset of snow melt and the progressive exposure of snow-free ground within the research area (see Fig. 2c). Wind speed showed pronounced variability during the campaign, with episodic increases exceeding 10 m s^{-1} indicating changes in synoptic conditions. Several periods were characterised by low CBH below 600 m a.s.l. or precipitation, occasionally limiting airborne operations. The observed changes in temperature and wind speed indicate variable boundary layer conditions throughout the campaign.

3 Measurement systems, instrumentation, and data post-processing

This section presents the configuration of the three different measurement systems that have been deployed in Ny-Ålesund during the field campaign in 2024. Furthermore, the subsequent data post-processing and quality control procedures are described. The three resulting data sets from the different measurement systems are publicly available on the world data centre PANGAEA (Felden et al., 2023).

3.1 Fixed-wing UAS ALADINA

3.1.1 Platform and instrumentation

The fixed-wing UAS ALADINA (**A**pplication of **L**ight-weight **A**ircraft for **D**etecting **IN**-situ **A**erosol) is based on the pusher aircraft type Carolo P360, which was designed and developed at Technische Universität (TU) Braunschweig. Since 2013, ALADINA has been deployed in multiple field experiments worldwide, with the main objective of investigating NPF and aerosol properties influenced by varying ABL conditions (e.g., Altstädter et al., 2015; Bärfuss et al., 2018; Harm-Altstädter et al., 2024; Lampert et al., 2020; Platis et al., 2016). For this purpose, it is equipped with a modifiable meteorological and aerosol payload of up to approximately 4.5 kg weight. The system features a wingspan of 3.6 m and a maximum take-off weight of 25 kg. To avoid any possible contamination compared to the use of a combustion engine, and to enable sufficient thrust for agile manoeuvring, the aircraft is powered by an electric engine with 5 kW. The duration of a measurement flight is typically about 40 min, and the cruising speed is kept constant at 28 m s^{-1} during automatic flight mode. To facilitate efficient field operations, batteries can be quickly and easily exchanged via a side cargo door, allowing for turnaround times of about

https://doi.org/10.5194/essd-2026-411
Preprint. Discussion started: 28 July 2026

Open Access Earth System Science Data Discussions

20 min between consecutive measurement flights. Safe operation is possible for wind speed up to 15 m s^{-1}, clear visibility and no precipitation. The most recent configuration of ALADINA is described in further detail in Harm-Altstädter et al. (2024), with the exception of a transponder, which was not included during the field campaign described here. Further information regarding sensor installation and validation can be found in Bärfuss et al. (2018).

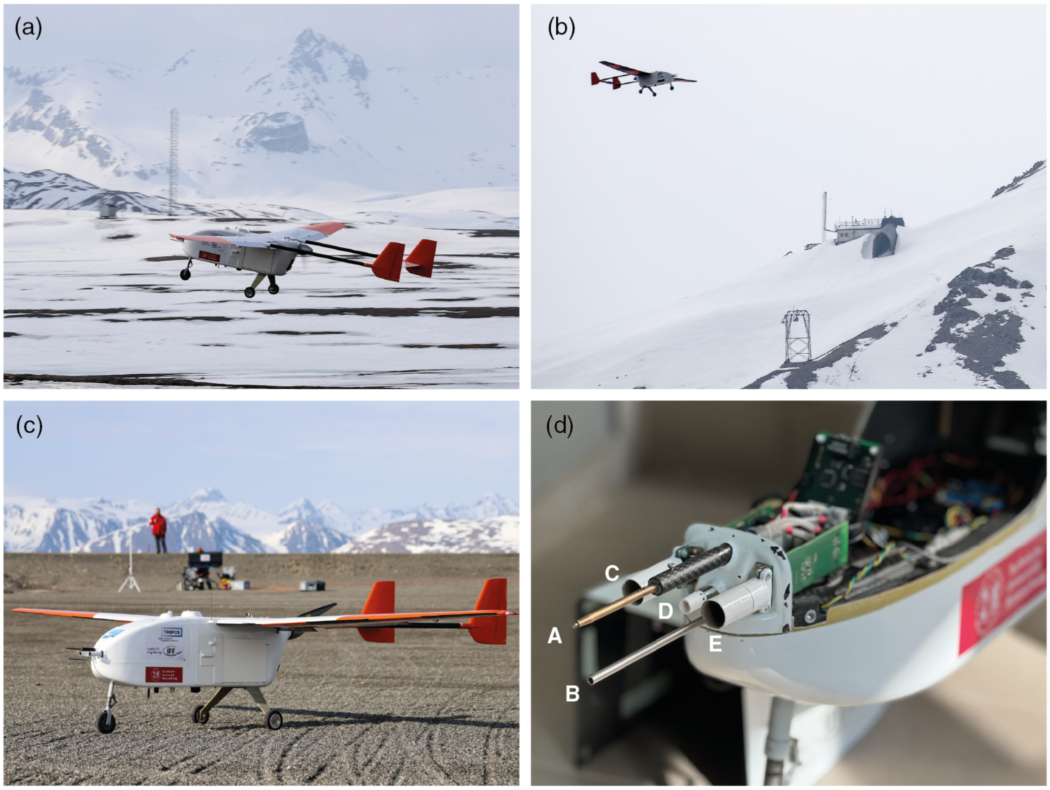

Figure 3. The fixed-wing UAS ALADINA during the field campaign in Ny-Ålesund in 2024. (a) ALADINA during take-off at the local airport on 1 June 2024, (b) during a measurement flight near the Zeppelin Observatory on 1 June 2024, (c) after landing, with the ground control station in the background on 3 June 2024, and (d) a picture showing the payload compartment and instrumentation mounted at the aircraft nose, including a multi-hole probe (A), the aerosol inlet (B), Finewire temperature sensor (C), HMP110 (D) and TSYS01/Rapid P14 (E) temperature and humidity sensors. (Pictures: TU Braunschweig)

In order to meet the high requirements posed by the challenging conditions in the Arctic, ALADINA has undergone several technical adaptations (Lampert et al., 2020) in preparation for a previous study in Ny-Ålesund in 2018 (Harm-Altstädter et al., 2023). A key modification is the insulation and active heating of the front payload compartment, which houses the meteorological instrumentation, and, in particular, the aerosol sensors that are sensitive to fluctuations in ambient temperature and humidity. The compartment is preheated and temperature-controlled prior to take-off and during flight to maintain an internal temperature of about 25 °C. As Ny-Ålesund is a radio-silent zone that prohibits the use of frequencies above 2 GHz, all telemetry links are configured to operate exclusively at 433 MHz and 868 MHz. The aircraft is remotely controlled during take-off

https://doi.org/10.5194/essd-2026-411
Preprint. Discussion started: 28 July 2026

and landing, using a Horus X12S (FrSky, China) and the redundant telemetry links EzUHF Rx at 433 MHz (ImmersionRC, Switzerland) and Archer RS at 868 MHz (FrSky, China), while a Pixhawk 2.1 Cube autopilot (CubePilot, Australia) is used during flight missions. Telemetry data are monitored at the ground control station using a RFD868s modem (RFDesign, Australia) and the MissionPlanner software. In addition, ALADINA is equipped with an inertial measurement unit (IMU) of type ADIS16488 (Analog Devices, USA) and a Global Navigation Satellite System (GNSS) module GPS16481 (Sparkfun, USA) with a receiver of type uBlox ZED-F9P (u-blox, Switzerland) to determine the attitude/orientation and position/altitude of the UAS. The GNSS data are also used to generate an accurate time standard for the measurement system. Both devices (IMU and GNSS) operate independently of the autopilot system, thereby providing redundant information on the aircraft's position and attitude during flight operations.

Figure 3 shows ALADINA during flight operation, as well as the meteorological sensors and the payload compartment. A more comprehensive overview of the measurement instrumentation deployed, including the calculated parameters and uncertainties provided by the manufacturers, is provided in Table 2. To sample the undisturbed airflow, the meteorological sensors and the aerosol inlet are mounted at the tip of the nose of ALADINA (see Fig. 3d). Three temperature sensors are installed, consisting of a platinum Finewire (FW) resistance thermometer with two measurement channels (Bärfuss et al., 2018), manufactured at the Institute of Flight Guidance (TU Braunschweig, Germany), a TSYS01 (Measurement Specialties, Ireland), both measuring at a fast temporal resolution of 100 Hz, as well as a HMP110 (Vaisala, Finland) with 1.7 Hz temporal resolution. Two distinct humidity sensors are integrated, covering a HMP110 (Vaisala, Finland) with 1.7 Hz temporal resolution, and a Rapid P14 (Innovative Sensor Technology, Switzerland) with < 1.5 s response time from 50 % to 0 % relative humidity at 23 °C. Two pyranometers of model ML-01 Si (Eko Instruments, Japan) are installed at the top and bottom of the fuselage to measure the up- and downwelling short-wave irradiance with a fast response time of less than 1 ms. In addition, a surface temperature sensor (MLX90614, Melexis, Belgium) is installed at the bottom of the fuselage with a field of view fixed to the aircraft body and temporal resolution of 100 Hz. A first calculation of wind speed (FF) and wind direction (DD) is determined from a multi-hole probe (TU Braunschweig, Germany) with AMS 5812 pressure sensors (Analog Microelectronics, Germany) and attitude information covering roll angle, pitch angle and heading of ALADINA from the Pixhawk 2.1 Cube autopilot system (see Sect. 3.1.2).

Furthermore, two condensation particle counters (CPC) of the same model 3007 (TSI, USA) are integrated in the payload compartment of ALADINA. The instruments were tuned in the laboratory of TROPOS by modifying the temperature difference between the saturator and the condenser, resulting in different lower cut-off sizes of 6 nm and 19 nm, respectively. The calibration of both CPC instruments at TROPOS is applied in accordance with the procedures described in Tuch et al. (2016) and Wiedensohler et al. (2018). The difference in the measured particle number concentrations between both sensors provides an identification of UFP for the size between 6 nm and 19 nm, hereafter named N_{6-19}. The uncertainty of N measured with both CPCs is given by the manufacturer with ±20 %. An optical particle counter (OPC) of type GT-526S (Met One Instruments, USA) is integrated below the two CPCs, measuring N for six different size channels between 300 nm and 10 μm, with a measurement uncertainty of ±15 %. The two CPCs and OPC use a critical orifice with a single pump to ensure a controlled airflow from the aerosol inlet towards the instruments (Harm-Altstädter et al., 2023). At a sufficient pressure difference between

https://doi.org/10.5194/essd-2026-411
Preprint. Discussion started: 28 July 2026

Table 2. Meteorological and aerosol instrumentation integrated in the UAS ALADINA for measurements of static temperature (T), relative humidity (RH), static pressure (p), wind speed (FF) and wind direction (DD), short-wave downwelling irradiance ($SW_{\downarrow}$) and upwelling irradiance ($SW_{\uparrow}$), surface temperature (T_S), and aerosol particle number concentration (N) in different size ranges from 6 nm to 10 μm.

Variable	Sensor (Manufacturer)	Sampling frequency	Measuring range		Uncertainty
T	Finewire (TU Braunschweig)	100 Hz	–		±0.1 K
	TSYS01 (Measurement Specialties)	100 Hz	-20 °C to +70 °C		±0.1 K
	HMP110 (Vaisala)	1.7 Hz	-40 °C to +80 °C		±0.4 K
RH	Rapid P14 (Innovative Sensor Technology)	100 Hz	0 % to 100 %		±1.5 %
	HMP110 (Vaisala)	1.7 Hz	0 % to 90 %	(-40 °C to 0 °C)	±3 %
			90 % to 100 %	(-40 °C to 0 °C)	±4 %
			0 % to 90 %	(0 °C to +40 °C)	±1.5 %
			90 % to 100 %	(0 °C to +40 °C)	±2.5 %
p	AMS 5812 (Analog Microelectronics)	100 Hz	758 hPa to 1207 hPa		±1 %
FF	AMS 5812 (Analog Microelectronics),	100 Hz, 25 Hz	–		±0.2 m s^{-1}
DD	Pixhawk 2.1 Cube (CubePilot)		–		depending on FF
$SW_{\downarrow}$	ML-01 Si (EKO Instruments)	100 Hz	0 W m^{-2} to 2000 W m^{-2}		±50 W m^{-2}
$SW_{\uparrow}$	ML-01 Si (EKO Instruments)	100 Hz	0 W m^{-2} to 2000 W m^{-2}		±50 W m^{-2}
T_S	MLX90614 (Melexis)	100 Hz	-70 °C to +380 °C		±0.5 K
N_6	CPC 3007 (TSI)	1 Hz	6 nm to 1 μm		±20 %
N_{19}	CPC 3007 (TSI)	1 Hz	19 nm to 1 μm		±20 %
N_{300}	OPC GT-526S (Met One Instruments)	1 Hz	0.3 μm to 0.5 μm		±15 %
N_{500}	OPC GT-526S (Met One Instruments)	1 Hz	0.5 μm to 0.7 μm		±15 %
N_{700}	OPC GT-526S (Met One Instruments)	1 Hz	0.7 μm to 1 μm		±15 %
N_{1000}	OPC GT-526S (Met One Instruments)	1 Hz	1 μm to 2.5 μm		±15 %
N_{2500}	OPC GT-526S (Met One Instruments)	1 Hz	2.5 μm to 5 μm		±15 %
N_{5000}	OPC GT-526S (Met One Instruments)	1 Hz	5 μm to 10 μm		±15 %

the pressure behind and in front of the orifice, the mass flow reaches a maximum and remains constant during measurement flights. The temporal resolution of both CPCs and OPC is 1 Hz.

3.1.2 Data processing and quality control

240 The data processing of ALADINA measurements is conducted individually for each flight. In general, data acquisition and time synchronisation of the overall measurement data from numerous sensors are achieved through a central bus system, operating at a sampling rate of 100 Hz, as shown in Bretschneider et al. (2022). To create a joint data set, including all measured variables, a common time axis of 100 Hz is defined with reference to Coordinated Universal Time (UTC), and used

https://doi.org/10.5194/essd-2026-411
Preprint. Discussion started: 28 July 2026

for synchronisation. The raw data readings are post-processed in several ways, as described below. Although there are multiple sources for identical atmospheric parameters, such as temperature and humidity, data are combined or validated by comparing individual sensor values, as shown in Bärfuss et al. (2018). Signal reconstruction and corrections are applied when necessary, as also demonstrated in Bärfuss et al. (2023). Measurements recorded at lower temporal resolution are included when available and gaps are retained as missing values. In addition to meteorological and aerosol variables, the final data set includes GNSS geolocation (latitude, longitude, altitude a.s.l., referenced to WGS84) and attitude information from the autopilot system (roll, pitch, heading).

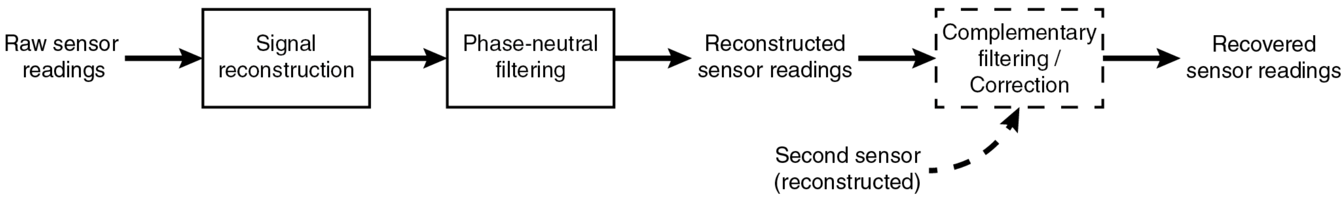

Figure 4. Generic data post-processing scheme applied to ALADINA raw sensor readings (e.g. temperature, humidity): signal reconstruction via inverted transfer function of first order, phase-neutral filtering, and optional individual correction and/or complementary fusion with a second sensor stream to obtain a recovered time series.

Temperature is derived from the two fast-response sensors TSYS01 and Finewire. The additional temperature measurements from HMP110 are not applied to the further processing of temperature data. To recover spectral errors and time lag in the raw sensor readings, several processing steps are applied to the raw measurements, as described in Bärfuss et al. (2023) and demonstrated in the block diagram in Fig. 4. First, the raw TSYS01 signal is reconstructed by applying an inverted transfer function of first order to the measured output. To identify a suitable time constant τ, representing the response time of TSYS01 during signal reconstruction, ascents and descents of different measurement flights are compared. Second, to reduce amplified noise during the first step, the reconstructed signal is phase-neutrally low-pass filtered forwards and backwards (Bärfuss et al., 2018). As a third step, and depending on the individual sensor, additional corrections or complementary filtering can be applied to the reconstructed sensor readings. Here, the potential bias from solar radiative heating on the TSYS01 measurements is identified when the angular separation between the sun direction (azimuth and elevation) and the ALADINA attitude (heading and pitch) is below 45°. Solar azimuth and elevation angles are derived from UTC time and the sun–earth geometry retrieved from the JPL Development Ephemeris DE405/LE405 (Standish, 1998). The resulting earth-centred inertial sun vector is transformed to local azimuth and elevation at the ALADINA GNSS position. The identified bias from solar radiative heating show maximum temperature increases of around 0.5 K in the TSYS01 measurements, depending on the weather conditions during measurement flights. No complementary filtering is applied for temperature, as the Finewire sensors demonstrate a stable fast response and no detectable bias from solar radiation through their design of two 0.0125 mm platinum wires. Instead of complementary filtering, the TSYS01 measurements are used as corresponding reference to validate and convert the raw sensor readings from the two Finewire channels into corrected temperature time series. A linear relationship is assumed and fitted between the raw Finewire sensor readings and the reconstructed temperature of TSYS01 during airborne conditions. Samples flagged for solar

https://doi.org/10.5194/essd-2026-411
Preprint. Discussion started: 28 July 2026

radiative heating are excluded during the calculations. The resulting Finewire temperature is quality checked by calculating the residual standard deviation relative to the TSYS01 reference. If both channels fail quality check, the reconstructed temperature of TSYS01 is used instead.

The temperatures measured by TSYS01 and the Finewire sensors represent the total air temperature at the stagnation point of ALADINA. The static air temperature is calculated using a simplified Mach number Ma based on the true airspeed and the total air temperature, following the procedure described in Bärfuss et al. (2023). The true airspeed is derived from the corrected dynamic pressure and dry-air density. The dry-air density is computed from the measured static pressure, the total air temperature, and the specific gas constant for dry air. Low-dynamic-pressure phases are excluded prior to the true airspeed calculation. The Mach number and the corresponding static air temperature are then calculated using the heat capacity ratio of air (κ = 1.4). This approximation introduces only a negligible error ($\ll$0.01 K) within the operating range of ALADINA, with cruising speed below 30 m s^{-1} (Ma < 0.1).

Humidity is based primarily on the Rapid P14 sensor and complemented by the HMP110 sensor. Analogous to the temperature processing, spectral errors and time lag in the Rapid P14 and HMP110 raw sensor readings are reconstructed by applying an inverted transfer function of first order followed by a phase-neutral low-pass filter (see Fig. 4). The time constant τ for the Rapid P14 sensor is determined by comparing ascents and descents of different measurement flights. In contrast, the HMP110 sensor shows a strongly affected response depending on the ambient temperature. Therefore, a temperature-dependent time constant is applied for the HMP110 reconstruction. First, suitable values of τ are identified by comparing ascents and descents of selected flights during measurement days with cold and warm ambient conditions. The median temperature at the top of the vertical profiles is used to establish a relationship between the identified time constants and the corresponding temperatures. Second, the Arrhenius equation is adapted to describe this relation between the HMP110 response time, represented by τ, and the temperature T (Arrhenius, 1889; Laidler, 1984):

$$\tau(T) = \tau_0 \exp\left(\frac{E_a}{RT}\right) \tag{1}$$

where τ_0 is a reference time constant, E_a the activation energy, R the universal gas constant, and T the measured temperature. The empirically determined HMP110 time constant and the fitted Arrhenius relationship are shown in Fig. 5b. The resulting time constant $\tau(T)$ is used for both, the first-order reconstruction, and the subsequent phase-neutral low-pass filtering of the HMP110 raw sensor readings. Prior to reconstruction, the HMP110 measurements are calibrated using a two-point salt-chamber calibration, while the Rapid P14 measurements are offset-calibrated against the calibrated HMP110 measurements using median values under non-saturated conditions. Finally, the relative humidity is obtained by complementary filtering of the calibrated and reconstructed Rapid P14 and HMP110 sensor readings, as described in detail in Bärfuss et al. (2018). For flights without valid Rapid P14 data, only the reconstructed humidity of HMP110 is used.

The horizontal wind vector is derived from the differential pressure measurements at the multi-hole probe together with the inertial navigation data of the autopilot system. The calculation is based on the vector difference between the velocity of the aircraft relative to the ground and the true airspeed vector relative to the moving air (Lenschow, 1972; Bärfuss et al., 2018; Bärfuss et al., 2023). To reduce noise, the horizontal wind components are subsequently low-pass filtered with a phase-

https://doi.org/10.5194/essd-2026-411
Preprint. Discussion started: 28 July 2026

neutral 20 Hz Butterworth filter, and wind direction (DD) and wind speed (FF) are recalculated from the filtered wind components. For flights with unstable autopilot attitude information, wind data are discarded for the entire measurement flight. The uncertainty of the calculated horizontal wind vector is ± 0.2 m s^{-1} in the horizontal plane. Consequently, the uncertainty of the wind direction DD depends on the wind speed FF, as shown in Fig. 5a. The two exemplary wind vectors illustrate the influence of wind speed on the uncertainty of the derived wind direction. At low wind speed below 0.5 m s^{-1}, the uncertainty of DD becomes increasingly dominated by the overall uncertainty of the horizontal wind vector, resulting in a strongly reduced significance of the derived wind direction.

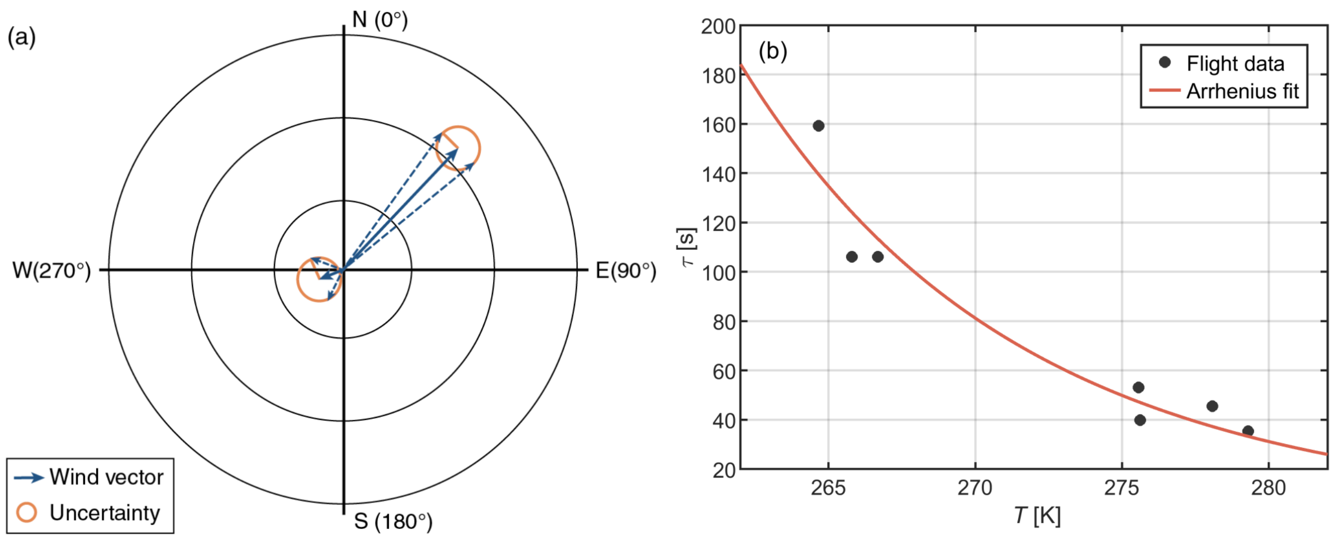

Figure 5. (a) Two exemplary horizontal wind vectors showing the dependence of the uncertainty in wind direction DD on the wind speed FF. The orange circles indicate the wind vector uncertainty of ± 0.2 m s^{-1} in any direction. The blue arrows indicate possible horizontal wind vectors within this uncertainty range. (b) Temperature dependence of the HMP110 response time constant τ. Black dots show empirically determined HMP110 time constants from selected cold and warm measurement flights, derived from ascent–descent comparisons. The red line shows the fitted Arrhenius function used for the HMP110 humidity reconstruction.

Short-wave downwelling and reflected irradiance are derived from the two ML01 sensors using fixed conversion factors based on manufacturer's specifications. The resulting short-wave irradiance is provided in W m^{-2}. The static pressure is measured by the AMS5812 pressure sensor and used to calculate the dry-air density and the static air temperature. The surface temperature is measured directly by the infrared sensor and is not subjected to further post-processing. For the final data set, each measurement flight is cropped to the periods covering the two scientifically relevant flight patterns in their vertical and horizontal extents (see Sect. 2.2). Flight phases in remote control, as well as calibration patterns before and after the measurement section are excluded. In addition, selected variables are discarded during turning manoeuvres, including curves within the vertical profiles. In particular, the aerosol particle number concentration N measured by the two CPCs 3007 shows enhanced variability during curve phases, possibly caused by effects of aircraft acceleration or sampling under side-slip con-

https://doi.org/10.5194/essd-2026-411
Preprint. Discussion started: 28 July 2026

ditions. Figure 6b demonstrates the affected measurement of N_6 during an exemplary vertical profile. The particle number concentration measured during turning manoeuvres (red line) exhibits substantially higher variability and is therefore treated as non-representative of the ambient aerosol field. Other variables excluded during turning manoeuvres are wind (FF and DD), short-wave irradiance $SW_{\downarrow}$ and $SW_{\uparrow}$, and surface temperature T_S, as the rapidly changing attitude of ALADINA during these phases may cause substantial variability and bias.

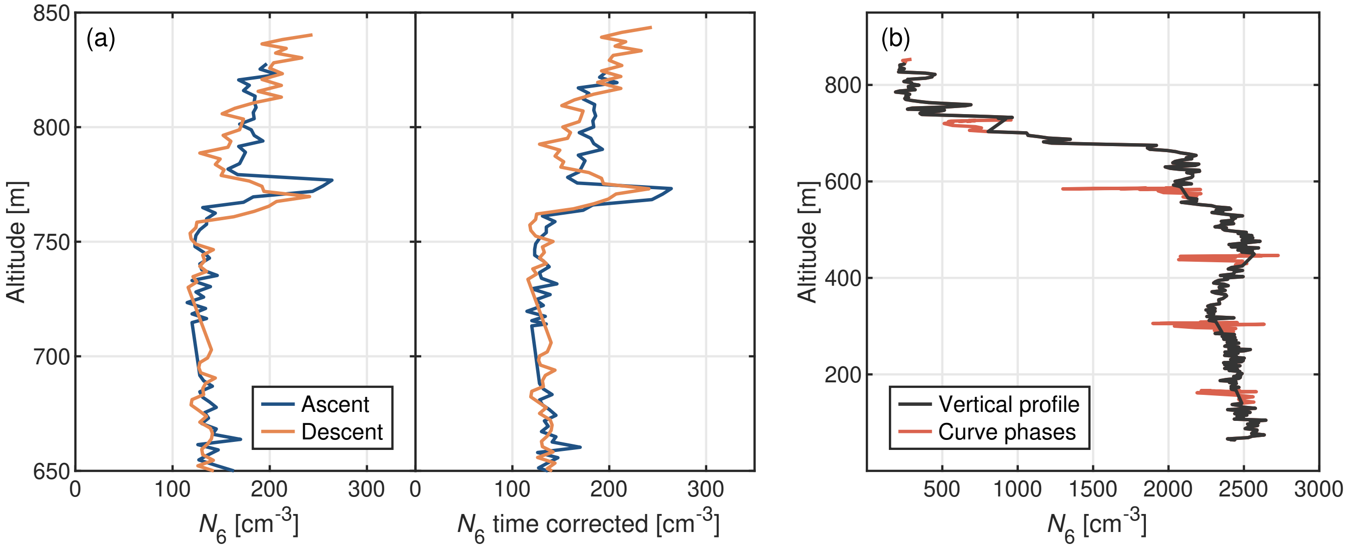

Figure 6. (a) Exemplary vertical profile of the particle number concentration N_6 during ascent and descent before (left) and after (right) application of the CPC time correction. (b) Exemplary vertical profile of N_6 with sections measured during turning manoeuvres highlighted in red. These curve phases show enhanced variability and are excluded from the final data set.

The aerosol particle number concentration N is post-processed by applying instrument-specific corrections. First, the raw data of the CPC sensors are calibrated using laboratory-determined detection efficiencies together with an additional mean sampling-efficiency factor of 1.05, determined for the particle size range from 40 nm to 500 nm. Second, the CPC concentration time series are corrected for the instrumental response time by applying a fixed negative time shift of 1.5 s, consistent with the findings of Altstädter et al. (2015). The response time correction is derived from the delay caused by flow velocity and tubing volume and by comparing ascents and descents from different measurement flights. Figure 6a shows an example of the measurement of N_6 before and after time correction. The uncorrected data show an ascent–descent offset in the vertical aerosol structure, consistent with the instrumental response delay. After time correction, the prominent concentration peak at approximately 770 m a.s.l. is aligned more closely between both profiles. Third, the calibrated aerosol number concentrations are converted to standard conditions (1013.25 hPa and 273.15 K), using the measured static pressure and the derived static air temperature. The OPC raw sensor readings are corrected for residence time and latency by applying a fixed negative time shift of 0.14 s, representing the response time induced by flow velocity and tubing volume. The resulting final data set provides synchronised meteorological, aerosol, and attitude-related variables for each measurement flight on a common UTC time axis.

3.2 Tethered balloon BELUGA

3.2.1 Platform and instrumentation

The BELUGA (**B**alloon-born**E** modu**L**ar **U**tility for profilin**G** the lower **A**tmosphere) system has been operated in the Arctic before, e.g., during the PASCAL (**P**hysical Feedbacks of **A**rctic Boundary Layer, **S**ea Ice, **C**loud and **A**eroso**L**) 2017 (Egerer et al., 2019) and MOSAiC (**M**ultidisciplinary drifting **O**bservatory for the **S**tudy of **A**rct**i**c **C**limate) 2020 (Pilz et al., 2023) campaigns. It consists of a 90 m^3 helium-filled tethered balloon operated by an electrical winch system and a tether-guiding pulley up to an altitude of 1.5 km. Different platforms with a total payload of up to 15 kg can be attached to the tether. During the field campaign in Ny-Ålesund presented here, three different payloads were used to measure vertical profiles of aerosol and meteorological parameters. The **T**urbulence **M**eteorological **P**robe (TMP) was used during all measurement flights in conjunction with one of the aerosol measuring platforms, either the **C**ubic **A**erosol **M**easurement **P**latform (CAMP) or the **m**iniaturized **S**canning **E**lectrical **M**obility **S**izer (mSEMS) box. The instrumentation of the three payloads is listed in Table 3. The mSEMS was used for the first time during this field campaign for potential further application as a balloon borne platform in cold environments. It was operated on four measurement flights conducted on 22 May 2024, 29 May 2024, 3 June 2024, and 6 June 2024. A detailed overview of the measurement days and sampling time is presented in Table 1. Here, a profile is defined as one ascent and one descent, while an entire flight is a measurement period with continuous data collection and no significant break, such as needed for battery exchange. The operation of the balloon depends on the meteorological conditions. The surface wind speed should not exceed 5 m s^{-1}, and wind speed throughout the vertical profile should remain below 15 m s^{-1}. The measured variables are monitored during flight operation. When prominent aerosol layers are detected, especially enhanced particle number concentrations in the UFP range, the focus of the flight is adjusted towards the corresponding altitude range to best characterise the level.

The Turbulence Meteorological Probe (TMP) is a development of TROPOS that is constantly being refined and adapted to specific requirements (see Fig. 7a). The TMP was previously used in an identical configuration during an expedition to Villum Research Station at Station Nord in northeast Greenland (Dorff et al., 2025). This version is designed to monitor standard meteorological parameters, such as wind speed, wind direction, temperature, humidity, and static pressure from which the barometric altitude is primarily determined. The aim of the TMP is to determine the meteorological parameters for scientific analysis and also to continuously monitor meteorological conditions to ensure flight safety. A small ultrasonic anemometer/thermometer (Trisonica mini, Li-Cor, USA) measures the three-dimensional wind vector and virtual temperature. According to the specifications provided by the manufacturer, the design of the Trisonica mini enables a horizontal inflow of $\pm 15°$. Due to the geometry of the instrument, it is not possible to accurately determine the vertical wind component. Therefore, only the absolute wind speed is used and it is assumed that the TMP's wind vane allows the system to be aligned with the mean wind. Alignment and attitude are determined using a three-dimensional compass (HMC6343, Honeywell, USA). The yaw angle then represents a measurement of the mean wind direction. Roll and pitch angles are only used to determine whether the probe and thus the Trisonica mini are still within the manufacturer's attitude range. Temperature, relative humidity, and static pressure are measured using a Graw radiosonde (DFM-17, Graw Radiosondes, Germany). The data structure of the DFM-17 is used to

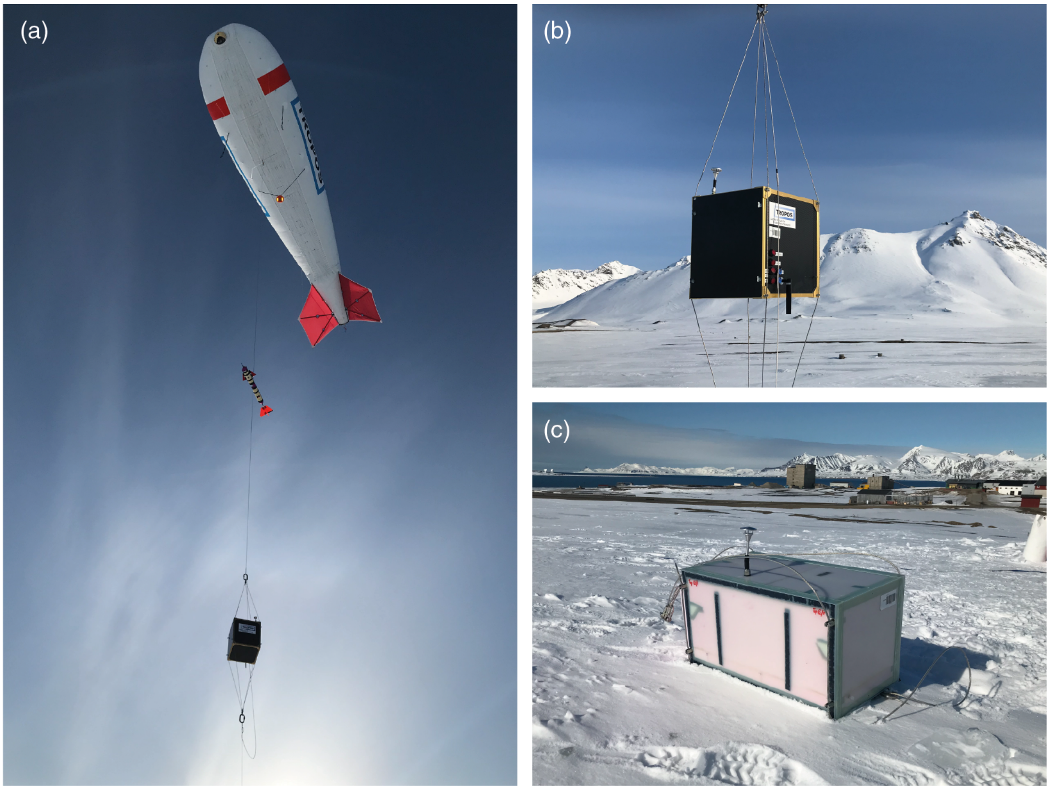

Figure 7. BELUGA measurement systems on 22 May 2024 during the field campaign in Ny-Ålesund. (a) TMP and CAMP attached to the tether line, (b) close-up picture of the CAMP system and (c) mSEMS box on ground on 22 May 2024. (Pictures: Christian Pilz, TROPOS)

integrate wind speed and direction from the Trisonica mini and the three-dimensional compass into the radiosonde's transmission protocol, thus enabling monitoring the flight operation from the ground. The meteorological observations are available with a temporal resolution of 1 Hz, which corresponds to an altitude resolution of about 0.5 m, valid for typical ascent rates of around 0.5 m s^{-1}. In addition, a one-dimensional hot-wire anemometer (Dantec Dynamics, Denmark) has been implemented for high-resolution turbulence measurements. The hot-wire anemometer is sampled at a rate between 50 Hz and 250 Hz. However, a malfunction in the data acquisition system has thus far prevented routine post-processing of the data, meaning that it can only be provided for a limited number of flights on request. Therefore, the hot-wire data is not included in the first release of the data set uploaded on PANGAEA.

The Cubic Aerosol Measurement Platform (CAMP) (Pilz et al., 2022) was developed for the operation on a balloon tether in cold atmospheric conditions (see Fig. 7b). The cubic box, which has a side length of 35 cm, is connected to carabiners via steel ropes at eight corners. This allows the system to be mounted on the tether line. The exterior walls are insulated and an internal heating system maintains the box temperature at about 25 °C to ensure stable measurement conditions. All instruments used in the CAMP sample from the identical steel vertical funnel inlet at the top of the box. The design of the inlet in combination with

https://doi.org/10.5194/essd-2026-411
Preprint. Discussion started: 28 July 2026

Table 3. Instrumentation of the TMP and the aerosol platforms CAMP and mSEMS used with BELUGA for measurements of static pressure (p), temperature (T), relative humidity (RH), wind direction (DD) and wind speed (FF), aerosol particle number concentration (N) with different lower cut-off sizes, and the aerosol particle number size distribution ($PNSD$) in different size ranges. For the TMP system, the measuring range and accuracy are based on the manufacturer's specifications.

Measurement system	Variable	Sensor (Manufacturer)	Sampling frequency	Measuring range	Uncertainty
TMP	p	DFM-17 (Graw)	1 Hz	1 hPa to 1100 hPa	±1 hPa
	T	DFM-17 (Graw)	1 Hz	-90 °C to + 60 °C	±0.2 °C
	RH	DFM-17 (Graw)	1 Hz	0 % to 100 %	±3 %
	DD	HMC6343 (Honeywell)	1 Hz	0° to 360°	± 5°
	FF	Trisonica mini (Li-Cor)	1 Hz	0 to 50 $\mathrm{m\,s^{-1}}$	±0.2 $\mathrm{m\,s^{-1}}$
CAMP	N_{11}	CPC 3007 (TSI)	1 Hz	11 nm to 1 μm	±20 %
	N_{15}	CPC 3007 (TSI)	1 Hz	15 nm to 1 μm	±20 %
	$PNSD$	POPS (Handix Scientific)	1 Hz	0.15 μm to 3 μm	±20 %
mSEMS box	N_9	CPC 3007 (TSI)	1 Hz	9 nm to 1 μm	±20 %
	$PNSD$	mSEMS (Brechtel)	1 min scan time	8 nm to 350 nm	±20 %

an overall flow rate of 1.4 m s^{-1} determines an upper particle cut-off of 2.7 μm at a wind speed of up to 3.5 m s^{-1}. The platform is equipped with two CPCs (model 3007, TSI, USA) with two different lower cut-off sizes of 11 nm (N_{11}) and 15 nm (N_{15}), measuring at a counting frequency of 1 Hz. The calculation of the counting efficiency of the CPCs is shown in Sect. 3.2.2. The initial flow system was replaced with an external vacuum pump and a customised critical orifice to set a constant sample flow rate of 0.11 l min^{-1}, reducing measurement uncertainty of the CPCs from ±20 % to ±5 %. A more detailed description of the CPC modification is presented by Pilz et al. (2022). Furthermore, a Portable Optical Particle Spectrometer (POPS, model 3100, Handix Scientific, USA) is integrated for measurements of the aerosol particle number size distribution ($PNSD$) (Gao et al., 2016). The POPS is a small and lightweight instrument that measures the single particle backscatter of a 405 nm diode laser, focused by a 38°–142°collection angle by a photomultiplier. The backscatter intensity is translated into an OPC particle number size distribution between 130 nm and 3 μm with a 1 Hz sampling frequency. For operation in the field, the sample flow of 0.46 l min^{-1} is controlled using a critical orifice and an external pump.

The second aerosol measuring platform mSEMS is designed similarly to the CAMP system and contains a CPC with a lower cut-off size of 9 nm (N_9) and the miniaturised Scanning Electrical Mobility Sizer (mSEMS, Model 9404, Brechtel Manufacturing Inc., USA). The mSEMS measures the mobility particle number size distribution in the range of 8 nm to 350 nm. A soft X-ray neutraliser (Model 5525-X, Grimm Aerosol Technik, Germany) is used to establish a defined charge distribution before selecting the particles for electrical mobility with the differential mobility analyser. The particles are counted with an advanced Mixing Condensation Particle Counter (aMCPC, Model 9403, Brechtel Manufacturing Inc., USA). The mSEMS

https://doi.org/10.5194/essd-2026-411
Preprint. Discussion started: 28 July 2026

was used with 30 size bins and a bin time of 2 s, resulting in a full up- or down-scan time of approximately 1 min through all channels. The mSEMS box has a size of 50 cm x 26 cm x 22 cm and weighs about 11.5 kg. Four steel cables, fixed to the aluminium framework, are used to attach the box to the tether, with two carabiners above and below. The instrument enclosure is formed by glass fibre composite plates of 0.5 mm thickness and 20 mm thick polystyrene foam insulation. Aerosols are sampled with a funnel inlet of the same geometry as used in CAMP and are dried with a custom silica-bead dryer. The barometric pressure, internal temperature, and relative humidity are recorded with a BME280 sensor (Bosch Sensortec GmbH, Germany). The sampled air temperature and relative humidity downstream of the dryer are monitored with a HYT221 sensor (B+B Thermo-Technik GmbH, Germany).

3.2.2 Data processing and quality control

The BELUGA measurements are divided into individual flights, whereby one flight describes a continuous measurement with a specific instrument setup and without long interruptions above 5 min. Measurement flights can include several ascents and descents. The altitude of the measurement systems is calculated using the isothermal hypsometric equation with the measured pressure values, respectively, as well as the ground pressure and temperature.

For the data post-processing of the TMP measurements, a rolling median is applied on five data points. Temperature measurements are additionally low-pass filtered to remove artificial spikes. It has been shown that the radiation protection of the integrated radiosonde sensors does not function optimally with certain orientations of the probe. Increased temperatures in the range of 2-5 K were measured due to direct sunlight. Consequently, all angles at which a temperature increase due to sunlight can occur are flagged, and the quality of the temperature measurements must be carefully considered on a case-by-case basis. This is relevant when the sonde exceeds a pitch value of more than 5°and the sonde's pointing direction is within ±45°of the sun's azimuth angle. Similarly, this is applied when the sonde's pitch angle exceeds -15°when pointing in the opposite direction within ±45°of the azimuth angle. This is not applied for cloudy measurement days or days with low solar radiation. Regarding wind speed measurements from the Trisonica mini, it is assumed that within a horizontal inflow of ±15°a proper functionality is guaranteed and that the calculated virtual temperature is valid within this range. The wind direction derived from the three-dimensional compass may contain increased uncertainties at low wind speed, as it is assumed that the TMP's wind vane aligns with mean wind direction.

In the CAMP platform, two CPCs are modified with respect to the temperature difference between the saturator and the condenser. Both instruments are calibrated using a reference electrometer with monodisperse silver aerosol particles of different sizes from 7 nm to 40 nm selected by a Differential Mobility Analyzer (DMA). The calibration method used is described in detail in Wiedensohler et al. (2018) and Tuch et al. (2016). As the CPCs internally calculate particle concentration from counts, the calibration includes additional, unknown corrections. The calibration process is thus able to compensate for any differences in the original flow rate. Consequently, the resulting calibration factors account for both the modified flow and the instrument's detection efficiency. Due to these corrections, the calculated counting efficiencies can exceed 100 %. The modified flow rates, measured during the campaign and laboratory volumetric flow values, demonstrate a strong correlation, with a mean discrepancy of ±6 %. A curve fit of the counting efficiency E, depending on the particle diameter D_p is estimated according

https://doi.org/10.5194/essd-2026-411
Preprint. Discussion started: 28 July 2026

Open Access
Earth System Science Data
Discussions

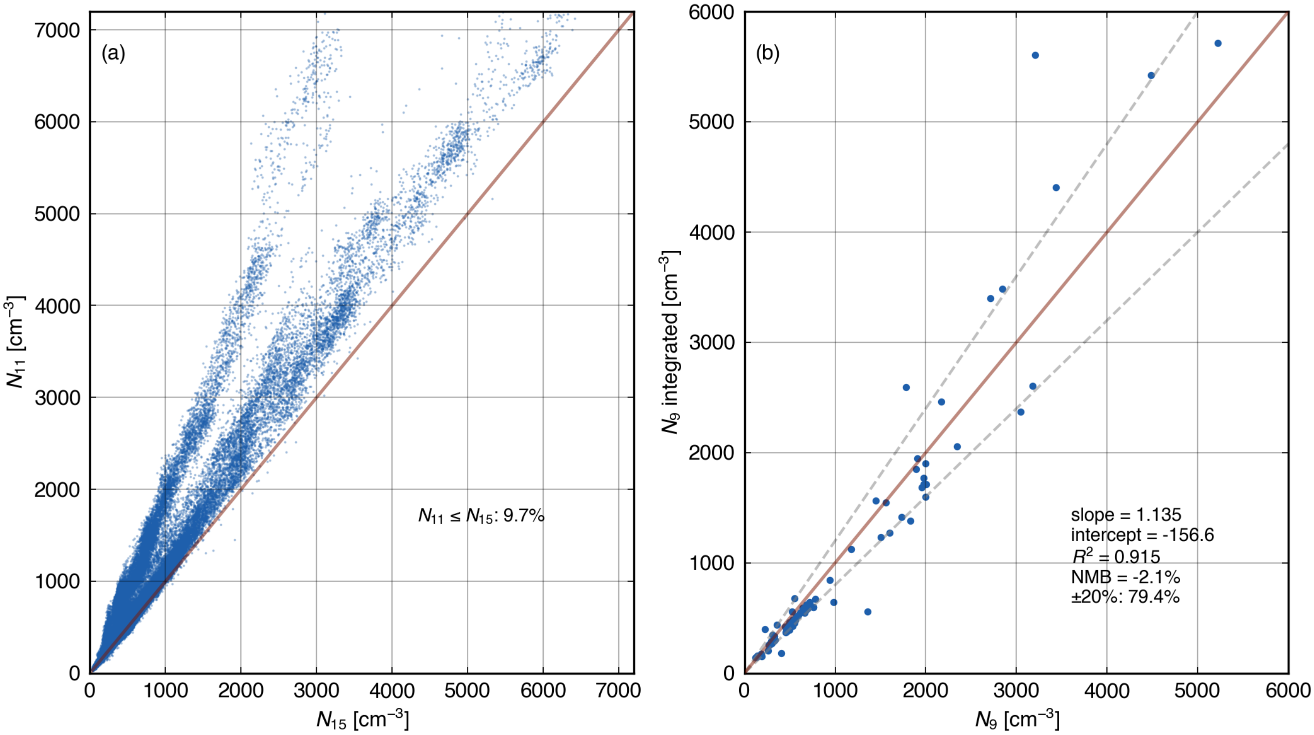

Figure 8. (a) All measurement point pairs of N_{11} and N_{15} obtained from the CAMP platform during the field campaign, showing the relation between the measurements of both CPCs with different lower cut-off size. (b) Integrated values of mSEMS measurements (9 nm to 350 nm) in comparison with 2 min mean of (N_9) used in the mSEMS box.

to

$$E = E_\infty \left(1 - exp\left(-\frac{D_p - D_{p0}}{D_{p50} - D_{p0}} \cdot ln(2)\right)\right), \qquad (2)$$

with D_{p50}, the particle diameter at which a 50 % efficiency is reached, which is the typical definition of the lower cut-off of the instrument (Tuch et al., 2016), and D_{p0} as the diameter with zero counting efficiency. The temperature difference between the saturator and the condenser of 15.1 K used in the first CPC led to a D_{p50} of 11 nm and the temperature difference of 9.5 K used in the second CPC led to a D_{p50} of 15 nm. Thus, the difference between both CPC measurements represents the particle number concentration from 11 nm to 15 nm (N_{11-15}). The values of N from both CPCs are additionally corrected for their respective plateau efficiency E_{oo}. The manufacturer specifies an upper limit of 1 μm, which is assumed here to define the upper cut-off for all CPC measurements. In combination with sampling losses at the inlet and in the tubing system, the CPC measuring N_{15} is corrected by a factor of 1.05 while the CPC measuring N_{11} is corrected by a factor of 0.94. As a last step, the corrected N from both CPCs is converted to standard conditions (1013.25 hPa and 273.15 K). For both CPCs, the manufacturer specifies an uncertainty range of ±20 %, which is reduced to ±5 % by flow stabilisation.

https://doi.org/10.5194/essd-2026-411
Preprint. Discussion started: 28 July 2026

Figure 8a shows the relationship between N_{11} and N_{15}, measured with the two CPCs during the field campaign. Due to their different cut-off sizes, N_{15} measurements should not exceed N_{11}, which is observed to apply for 90.3 % of the measurement data. This verifies the reliability of the measurements in estimating N_{11-15} in the ultrafine particle regime. In addition to the two CPCs installed in the CAMP platform, a POPS provides measurements of the $PNSD$. Size calibrations for the different channels of the POPS are applied using spherical polystyrene latex (PSL) particles in 13 sizes ranging from 0.125 μm to 3 μm. The calibration procedure is described in detail by Pilz et al. (2022). It has been shown that the background noise below 150 nm is relevant under clean conditions. Therefore, only size channels larger than 150 nm are used for further analysis. The integration over all size channels above 150 nm results in a particle number concentration hereafter named N_{150} (Pilz et al., 2022).

For the mSEMS box, the size-resolved sampling efficiency is determined for the aMCPC in a laboratory calibration, and correction factors are applied accordingly. Similarly to the previously described post-processing of CPC measurements, corrections are applied to the CPC used in the mSEMS box (correction factor 0.72 and a D_{p50} of 9 nm) and the corrected N is converted to standard conditions. Data inversion on $PNSD$ is performed using the manufacturer's script to account for doubly charged particles. Up- and down-scans are then averaged over concentration, resulting in an effective scan frequency of 2 min for the final data set. Figure 8b presents a comparison of the integrated $PNSD$ from the mSEMS with N_9 obtained from the CPC of the mSEMS box. Both measurement data demonstrate a strong correlation (R^2 of 0.915), with 80 % of the measurements falling within a range of $\pm$20 % of each other.

3.3 Surface flux gradient system

3.3.1 Platform and instrumentation

Profile measurements with the surface flux gradient system (Mathes et al., 2025a), hereafter referred to as the gradient system, were carried out on 13 different days (see Table 1). The sampling time per day varied from 6 h to 23 h. The derived data are divided into three categories based on the surface coverage with snow:

1) Snow: surface is fully covered with snow or ice (see Fig. 9a).
2) Snow and vegetation: snow patches and patches with open tundra vegetation (see Fig. 9b).
3) Vegetation: snow is fully melted, tundra vegetation is dominant (see Fig. 9c).

To measure near-surface aerosol particle number concentration profiles, a 1.5 m high linear actuator is used with a sensor board (see Fig. 9d). A 20 cm long, downward-facing stainless steel inlet with an inner diameter of 3 mm is mounted on the sensor board. The inlet is connected to a CPC (model 3007, TSI, USA) via a 205 cm long conductive silicon tube with an inner diameter of 4.2 mm. The CPC measures N with a lower cut-off diameter of 10 nm at a sampling frequency of 1 Hz and with a sample volume flow rate of 0.7 l min^{-1} (see Table 4). In addition to the aerosol inlet (I) shown in Fig. 9d, the sensor board contains a simple hot wire anemometer (Rev. P., Modern Device, USA) to measure wind speed and temperature (Fig. 9d, II), and an ultrasonic distance sensor (UC2000-30GM-E6R2-V15, Pepperl and Fuchs, Germany) to measure the distance to the

https://doi.org/10.5194/essd-2026-411
Preprint. Discussion started: 28 July 2026

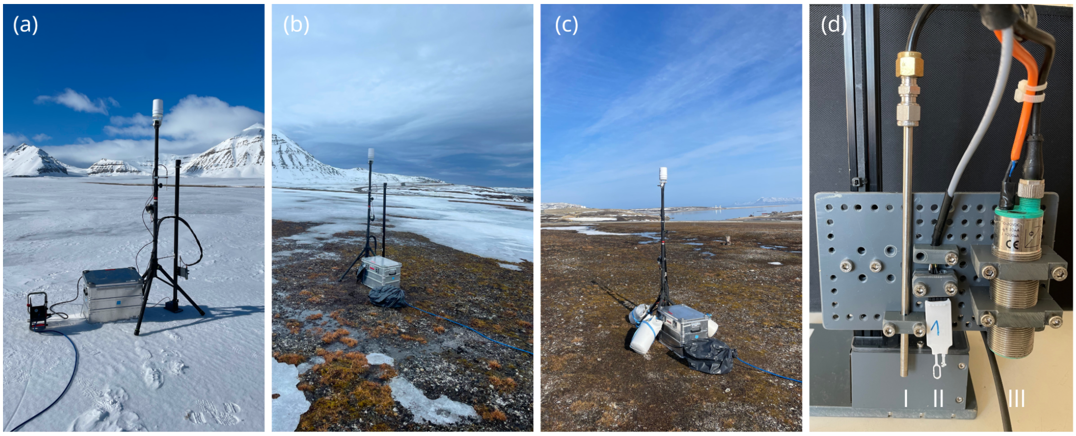

Figure 9. Three pictures of the studied surface types during the field campaign in Ny-Ålesund. (a) Snow on 22 May 2024, (b) Snow and vegetation on 30 May 2024, (c) Vegetation on 5 June 2024, and the (d) sensor board of the gradient system: (I) aerosol inlet, (II) hot wire anemometer and the (III) distance sensor. The sensor board was attached to the linear actuator. (Pictures: Theresa Mathes, TU Berlin)

surface (Fig. 9d, III). These sensors are operated with a sampling frequency of 1 Hz (see Table 4). The linear actuator and all sensors are operated via a 24 V power connection. A laptop for system control and data recording, and the CPC were placed downwind of the gradient system in an aluminium box for weather protection during the field campaign. The gradient system was realigned into the wind when the wind direction changed, and was predominantly located upwind of the BELUGA ground station due to the prevailing northwest and southeast main wind directions. A tripod was used to stabilise the system and was positioned downwind of the gradient system. During periods of high wind speed, exceeding 6 m s^{-1}, the gradient system was stabilised using sandbags.

Meteorological parameters, including wind direction and wind speed, temperature, relative humidity, precipitation and solar irradiance, were measured using a weather station (Atmos 41, METER, USA) installed at the top of the tripod (2 m height, see Fig. 4). The gradient system was programmed to sequentially sample at six distinct height levels automatically, beginning at 10 cm above the surface and followed by the heights of 14, 22, 38, 69 and 134 cm. The actual sampling heights varied by ± 1 cm, depending on measurement conditions (e.g. snowfall) and surface characteristics. During the downward movement from 134 cm back to 10 cm, an additional measurement was taken at the height of 38 cm. This served as a reference point to monitor potential changes in background particle number concentration but is not included in the gradient calculation. Each height level was sampled for 50 s, resulting in a complete vertical profile every 350 s.

3.3.2 Data processing and quality control

The data post-processing and data analysis of the gradient system proceed in a series of steps. Firstly, the height level of the gradient system is verified using data from the distance sensor. A measured profile is included in the subsequent analysis if more than 80 % of the height measurements at each level are within ± 20 % of the respective set point. The CPC required up

https://doi.org/10.5194/essd-2026-411
Preprint. Discussion started: 28 July 2026

Table 4. Instrumentation used at the near-surface gradient system for measurements of temperature (T), relative humidity (RH), short-wave irradiance (I), precipitation (P), wind direction and speed (DD, FF), aerosol number concentration (N_{10}), and distance to the surface (d).

Variable	Sensor (Manufacturer)	Sampling frequency	Measuring range	Uncertainty
T	Hot Wire Anemometer (Rev. P, Modern Device)	1 Hz	–	–
	ATMOS 41 (METER)	0.1 Hz	-50 °C to 60 °C	±0.6 °C
RH	ATMOS 41 (METER)	0.1 Hz	0 % to 100 %	±3 %
I	ATMOS 41 (METER)	0.1 Hz	0 to 1750 W m^{-2}	±5 %
P	ATMOS 41 (METER)	0.1 Hz	0 to 1500 mm h^{-1}	±5 %
FF, DD	ATMOS 41 (METER)	0.1 Hz	0 to 30 m s^{-1}, 0°–360°	±3 %, ±5°
	Hot Wire Anemometer (Rev. P, Modern Device)	1 Hz	–	–
N_{10}	CPC 3007 (TSI)	1 Hz	$>$ 10 nm to 1 μm	20 %
d	UC2000-30GM-E6R2-V15 (Pepperl & Fuchs)	1 Hz	80 mm to 2000 mm	–

to 9 s to fully adjust to a change in particle number concentration, and the vertical movement between levels required up to 10 s. Therefore, the final 30 s of each 50 s measurement interval, during which the CPC has reached a stable response and the system was no longer moving, are used for further analysis. Secondly, outliers are removed if values are outside 1.5 times the interquartile range within a moving window of 20 min. This specific time period is selected to mitigate the impact of short-term fluctuations while still capturing long-term trends. The arithmetic mean over the 30 s measurement interval is then calculated for each height level. Thirdly, wind speed and temperature from the hot-wire anemometer are compared to measurements from the weather station, which is located at the top of the gradient system at 200 cm a.g.l. To avoid flow distortion caused by obstacles, data from a 90° wind sector centred on the instrument tripod and the equipment box containing the logging system are excluded from the analysis. Furthermore, time periods that have potentially been influenced by local pollution, characterised by a rapid increase in particle number concentration, are excluded from the analysis. A logarithmic wind profile with height is assumed, as all measurement levels are within the surface (Prandtl) layer. Based on a linear regression of wind speed against the logarithm of height, hot-wire anemometer data are extrapolated to the 200 cm reference height. A correction factor is derived based on the calculated offsets, and all data are adjusted accordingly. Consequently, the corrected hot-wire anemometer data are used in further analyses.

The measured N is calibrated by applying detection efficiencies derived from a reference electrometer with monodisperse silver aerosol of different sizes from 5 nm to 40 nm. Additionally, the measured particle number concentration is adjusted for losses that occurred in the inlet system and sampling lines, particularly diffusional losses of small particles to the inner walls of the tubing and inlet surfaces (Kulkarni et al., 2011). These losses are estimated as described by Gormley and Kennedy (1949). To determine the particle penetration efficiency as a function of particle size, N in the size range from 12 nm to 573 nm is used. Measurements of the $PNSD$ from a Neutral Cluster and Air Ion Spectrometer (NAIS, Airel, Estonia) are used for the size range from 12 nm to 37 nm (Boyer, 2025), and for the size range from 37 nm to 573 nm, measurements from

https://doi.org/10.5194/essd-2026-411
Preprint. Discussion started: 28 July 2026

Earth System Science Data
Open Access Discussions

a scanning mobility particle sizer (SMPS model 3034, TSI, USA) are used. Both instruments are located at the Gruvebadet Atmosphere Laboratory. The obtained particle concentration in the positive and negative charging mode from the NAIS are averaged. It is assumed that the measured $PNSD$ from the NAIS and SMPS are representative of the measurements of the gradient system, as direct measurements of the particle size distribution at the location of the gradient system are not available. The corresponding sampling loss rate is calculated for each size bin of the NAIS and SMPS based on the inlet characteristics described in Sect. 3.3.1. The size dependent loss rates are then multiplied by the normalised $PNSD$ from the NAIS and SMPS, and the total particle penetration efficiency is estimated by summing up the number-weighted particle penetration efficiencies in the considered size range. When $PNSD$ data from the NAIS or SMPS are unavailable, the daily mean penetration efficiency is used instead. The median particle penetration efficiency for one hour intervals ranged from 85 % to 99 %, with an overall median of 98 %. This variability reflects the strong dependence of particle losses on size (Kulkarni et al., 2011).

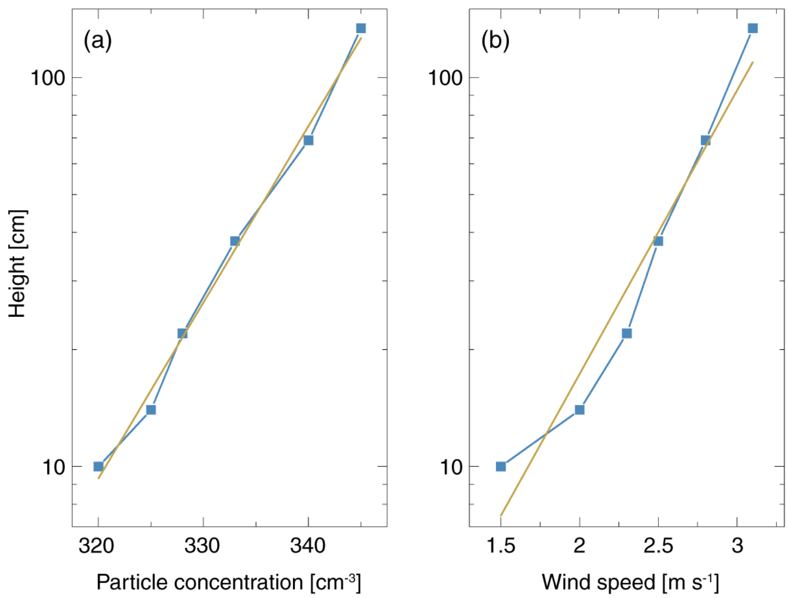

Figure 10. Illustrative example of vertical profiles of (a) particle concentration N [cm^{-3}] and (b) wind speed FF [m s^{-1}]. The beige line shows the linear regression fit, with R^2 of 0.99 for the particle concentration gradient and R^2 of 0.97 for the wind speed gradient.

When evaluating gradients based on ascending stepped profiles, only intervals are considered in which at least four of the six height levels show valid measurements. Figure 10 provides an illustrative example of the measurements of the gradient system used in the subsequent data analysis, showing exemplary profiles of N and wind speed FF, as well as linear regression fits. In the surface layer, turbulent fluxes, such as momentum flux ($\overline{U'w'}$), sensible heat flux ($H = \overline{w'T'}$), and particle number flux ($P = \overline{w'C'}$) are often related to vertical gradients of particle number concentration N, horizontal wind speed FF, and temperature T (Holton and Hakim, 2013; Foken and Mauder, 2024). A comprehensive description of this relationship is presented

https://doi.org/10.5194/essd-2026-411
Preprint. Discussion started: 28 July 2026

in the study of Mathes et al. (2025a). Assuming equal eddy diffusivities ($K_m = K_H = K_P$) under neutral stratification (e.g., Wieringa, 1980; Held et al., 2011), and with the von Karman constant $\kappa = 0.4$, the friction velocity u_* is used to express:

$$u_* = \kappa \frac{\partial U}{\partial \ln z} \qquad [\mathrm{m\ s^{-1}}] \tag{3}$$

The friction velocity u_* is determined according to Eq. (3) from the measured vertical gradient of the horizontal wind speed FF using a linear regression of five wind speed measurements against the logarithm of the respective heights. In the same way, vertical gradients of air temperature T and particle number concentration N_{10} are obtained from linear regressions and used to estimate the corresponding sensible heat flux H (Eq. (4)) and particle flux P (Eq. (5)).

$$H = -\kappa \cdot u_* \cdot \frac{\partial T}{\partial \ln z} \qquad [\mathrm{W\ m^{-2}}] \tag{4}$$

$$P = -\kappa \cdot u_* \cdot \frac{\partial N_{10}}{\partial \ln z} \qquad [10^6\ \mathrm{m^{-2}\ s^{-1}}] \tag{5}$$

Positive values of H indicate an upward flux, i.e. when the calculated temperature decreases with height. Similarly, a positive P denotes an upward flux of particles, when particle concentration decreases with height. The particle and sensible heat fluxes are evaluated in 20 min intervals (see Eqs. (4) and (5)). A temporal linear regression is applied to obtain corresponding values of particle number concentration, wind speed, and temperature at the median timestamp for each interval. Figure 11 shows a 20 min interval with four profiles of particle concentration and wind speed. In this example, the interval starts at 12:09 UTC on 8 June 2024 and ends at 12:31 UTC on 8 June 2024 with four to six different height levels per profile. All heights are interpolated for a median timestamp at 12:20 UTC. The calculated u_* is 0.14 m s^{-1}, with a net P of 0.98 10^6 m^{-2} s^{-1}.

To exclude intervals with weak turbulence and potential decoupling, especially relevant under stable conditions or above snow and ice surfaces, fluxes are only calculated for profiles with friction velocity $u_* \geq 0.15$ m s^{-1}. Additionally, data were quality checked during the regression analysis for the flux calculation to ensure that only values based on an R-squared $\geq$ 0.5 are included. The majority of measurements were taken under near-neutral stratification conditions, with interquartile range values of $-0.235 < z/L < 0.005$. Therefore, stability corrections are neglected, with a maximum estimated error below 11 % (Businger et al., 1971). Uncertainties in flux estimates due to measurement uncertainty are assessed using Monte Carlo simulations. For each profile, 10,000 iterations are generated using Gaussian-distributed noise. The assumed standard deviations are 20 % for particle concentration according to the manufacturer, 5 % for temperature, and 0.5 m s^{-1} for wind speed (Prohasky and Watkins, 2014). Fluxes are recalculated for each ensemble, and the 90$^{\text{th}}$ percentile is taken as the uncertainty range (Watanabe and Pfeiffer, 2022). The resulting absolute median uncertainties are 17 W m^{-2} (standard deviation (SD) ±38) for H and 0.70 × 10^6 m^{-2} s^{-1} (SD ±7.21) for P. A more detailed description of the applied method and its validation is provided in Mathes et al. (2025a).

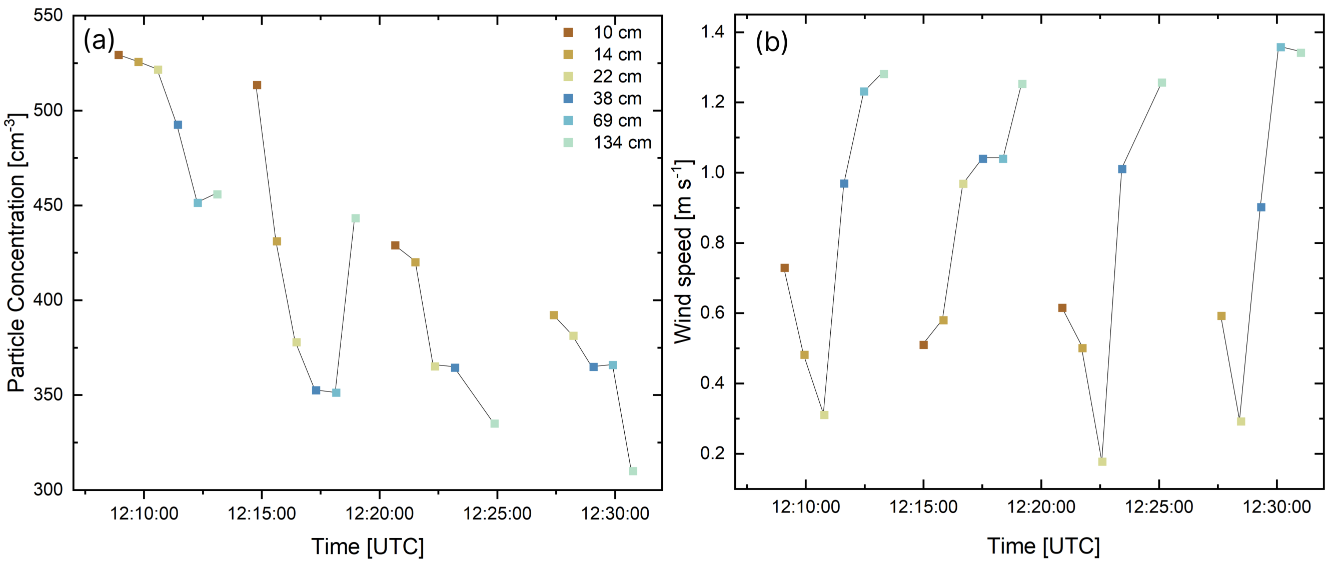

Figure 11. Time series of (a) particle concentration N [cm^{-3}] and (b) wind speed FF [m s^{-1}] derived from multiple profiles of the gradient system in a 20 min interval on 8 June 2024. The different colours show the height of the measurement.

4 Combined airborne and surface-based observations on 3 June 2024

In this section, the measurements obtained from all three systems on 3 June 2024 are presented as a representative case study, demonstrating the potential of the combined observations to investigate aerosol variability in interaction with boundary-layer and surface exchange processes. Throughout the measurement day, ALADINA was operated between 09:15 UTC and 19:34 UTC, conducted 21 vertical profiles and nine horizontal patterns. BELUGA was operated between 09:12 UTC and 18:11 UTC, resulting in eight vertical profiles. The surface flux gradient system was in operation starting at 00 UTC, with the exception of a time period between 08:50 UTC and 12:00 UTC.

To provide a broader campaign context for the observations from 3 June 2024, Fig. 12 presents overall campaign vertical statistics of potential temperature θ, specific humidity q and aerosol particle number concentration N, derived from all available ALADINA and BELUGA vertical profiles. The median profiles illustrate the range of thermodynamic and aerosol conditions observed during the field campaign, and are not intended as a direct platform comparison. This is important because ALADINA and BELUGA were not always operated simultaneously or on the same day due to operational limitations (see Sect. 2.2). In addition, the two systems covered different altitude ranges, operated at different locations in the vicinity of Ny-Ålesund, and sampled different meteorological regimes during the campaign, including cold conditions and periods affected by snow melt (see Sect. 2.2). For all three parameters shown in Fig. 12, the interquartile ranges underline the variability of the meteorological conditions observed during the field campaign.

Both airborne systems demonstrate an increase in potential temperature θ with altitude, indicating predominantly stable stratification in the measured lower atmosphere. The specific humidity q either decreased with altitude (BELUGA) or remained

https://doi.org/10.5194/essd-2026-411
Preprint. Discussion started: 28 July 2026

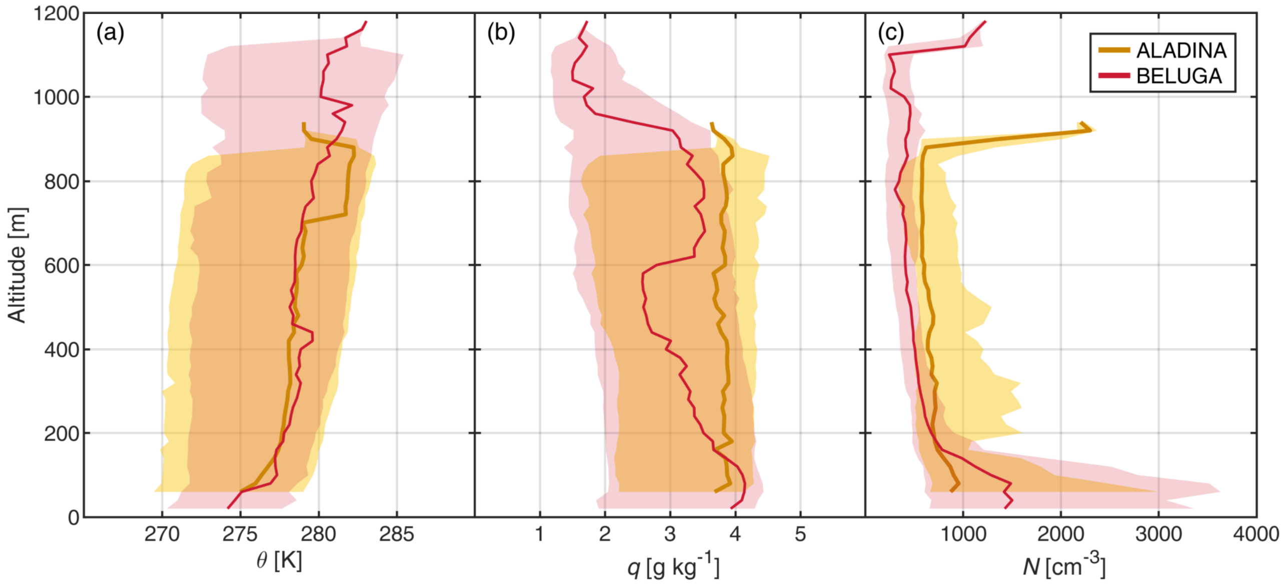

Figure 12. Median profiles derived from all available ALADINA and BELUGA vertical profiles during the field campaign: (a) potential temperature θ, (b) specific humidity q and (c) aerosol particle number concentration N. The profiles were calculated for each airborne system in 20 m altitude bins, with shaded areas indicating the interquartile range between the 25th and 75th percentiles of the measured values. For the aerosol profiles, N_6 was used for ALADINA and N_{11} for BELUGA where available.

nearly constant within the altitude range (ALADINA), indicating that vertical humidity gradients were not uniform across the campaign period. The increased median values in the BELUGA profile of q near the surface suggest that enhanced moisture content was confined to lower altitudes, likely due to stable stratification and periods affected by snow melt during measurement days after 28 May 2024, while drier conditions occurred at higher altitudes. Furthermore, elevated values of q between 600 m and 900 m a.s.l. in the BELUGA profile may correspond to cloud-influenced layers aloft. Observations over a period of 25 years in Ny-Ålesund demonstrated that the median cloud base height during the spring and summer seasons frequently remained at altitudes below 1 km (Maturilli and Ebell, 2018). This is not captured by the ALADINA measurements due to the operation under cloud-free conditions. The aerosol particle number concentrations show pronounced vertical variability, with differences between the two airborne systems partly related to the different lower cut-off diameters used for N and to the variability of aerosol conditions observed on different measurement days. The enhanced concentrations observed at elevated altitudes may be influenced by differences in altitude coverage among the individual measurement flights, as not every profile reached the maximum altitude. At the same time, increased N below 180 m a.s.l. coincides with a pronounced surface-based inversion layer visible in the median profiles of θ. Observations during a previous field campaign in Ny-Ålesund in 2018 similarly showed increased values of N below 300 m a.s.l. (Harm-Altstädter et al., 2023). Overall, the campaign-wide profiles provide a reference for interpreting the thermodynamic and aerosol observations obtained on 3 June 2024.

https://doi.org/10.5194/essd-2026-411
Preprint. Discussion started: 28 July 2026

Open Access Earth System Science Data Discussions

The prevailing meteorological surface conditions during the selected case study day are shown in Fig. 13 and include wind speed and direction, temperature and short-wave downward irradiance (adapted from: Maturilli, 2020a, b). During the measurement period, near-surface wind speed increased notably after 10:00 UTC and remained elevated until approximately 16:00 UTC, reaching up to approximately 6 m s^{-1}. At the same time, the wind direction changed from variable conditions at low wind speed to a more persistent wind direction, ranging from East to Southeast as the wind speed increased. The air temperature remained consistently above 4 °C throughout the day. The pronounced temporal variability in downward short-wave irradiance indicates the occurrence of alternating periods of clear sky conditions and cloud cover.

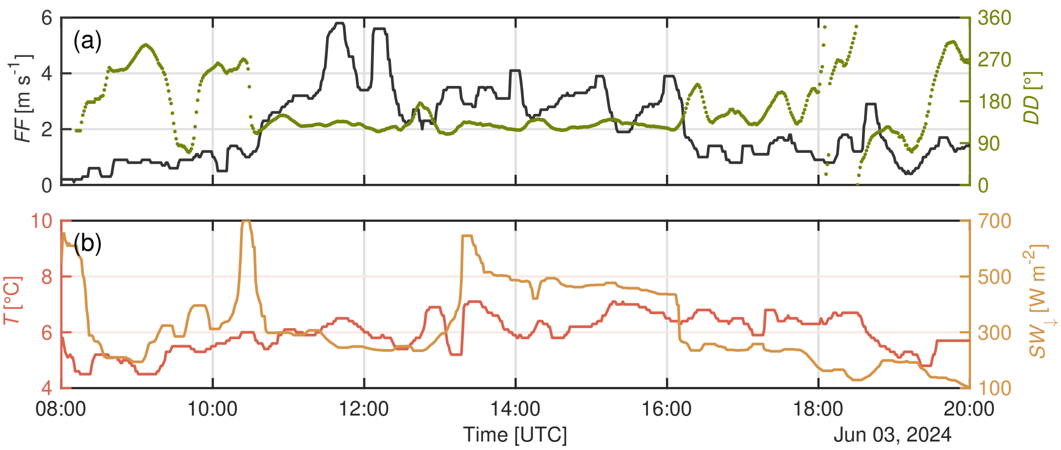

Figure 13. Time series of selected surface meteorological parameters in 15 min intervals, derived from AWIPEV Research Base during the measurement period on 3 June 2024. (a) Wind speed (FF, m s^{-1}, black line) and wind direction (DD, °, green dots) both at 10 m a.g.l. (b) air temperature (T, °C, red line) at 10 m a.g.l. and short-wave downward irradiance ($SW_{\downarrow}$, W m^{-2}, amber line).

The sensible heat flux H and particle flux P on 3 June 2024, derived from the measurements of the surface flux gradient system, are presented in Fig. 14. The surface area at the measurement site was clear of snow, although a small snowfield was present at a distance of approximately 10 m, orientated upwind in the main wind direction (see Fig. 9b). The results show a net upward H during 75 % of the day (see Fig. 14a), with an average flux of 25 W m^{-2} for the net positive flux intervals. Taking the potential uncertainties represented by the grey error bars in Fig. 14 into account, the sensible heat fluxes are mostly positive. H reached an average flux of 53 W m^{-2} between 12:00 UTC and 18:00 UTC. The positive H coincides with a clearing of cloud cover and an increase in short-wave downward irradiance, which increased from approximately 250 W m^{-2} to over 500 W m^{-2} during this measurement interval. In addition, an increase in temperature was observed during this period reaching a daily maximum of 6.9 °C at 18:00 UTC at the gradient system measurement site. Concurrently, increasing wind speed during this period resulted in an increase of friction velocity to 0.2 m s^{-1}. With regard to particle flux (see Fig. 14b), deposition intervals predominated for 61 % of the day. The most pronounced flux occurred between 13:00 UTC and 17:00 UTC, with a net particle deposition flux of -1.04 10^6 m^{-2} s^{-1}. During this interval, the aerosol number concentration N_{10} increased to 1,040 cm^{-3} at the gradient system measurement site, compared to an average of 940 cm^{-3} for the rest of the day. It is possible

https://doi.org/10.5194/essd-2026-411
Preprint. Discussion started: 28 July 2026

Earth System Science Data
Open Access Discussions

that the shift in wind direction after 10 UTC from variable conditions to Southeast along with increasing wind speed led to a change in air masses, which may have contributed to the observed net particle deposition. This transition was accompanied by an increase in friction velocity (u_*), potentially enhancing deposition processes. Conversely, the melting of the snow or drying of the tundra due to higher solar irradiance and higher temperature probably leads to an increase in sensible heat flux.

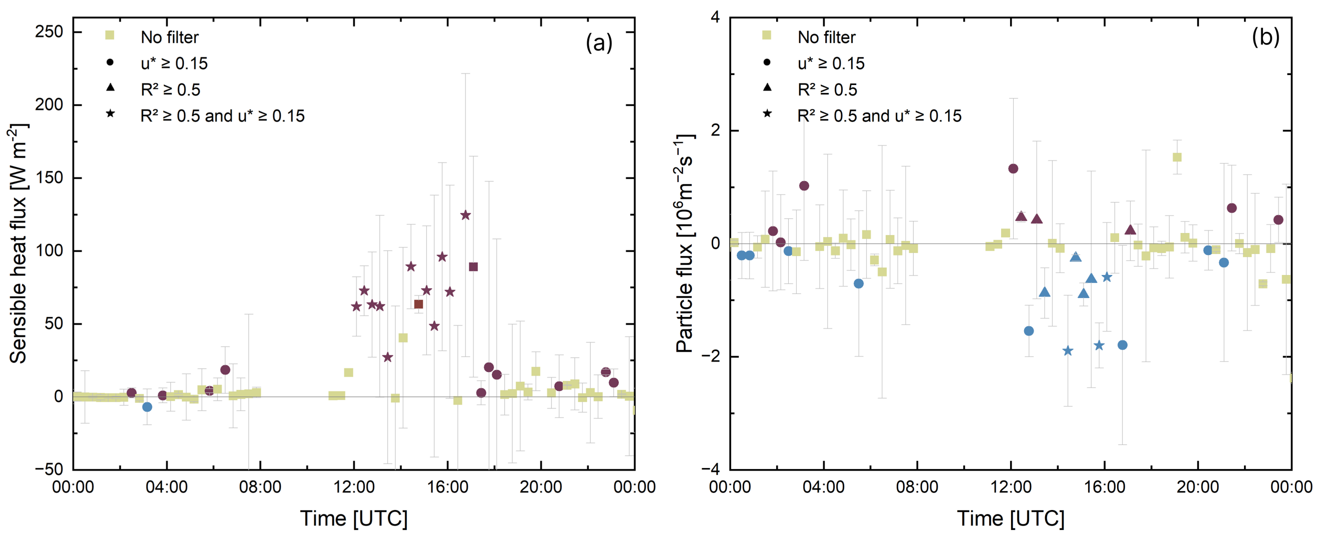

Figure 14. (a) Sensible heat flux (H, W m^{-2}) and (b) particle flux (P, 10^6 m^{-2} s^{-1}) calculated from measurements of the surface flux gradient system on 3 June 2024 with surface type Snow and Vegetation. The brown colour indicates net positive flux intervals, and the blue colour indicates net negative flux intervals. The beige colour indicates intervals with $u_* < 0.15$ m s^{-1} or $R^2 < 0.5$. The circle shows intervals with $u_* \geq 0.15$ m s^{-1}, the triangle when $R^2 \geq 0.5$, and the star when both conditions are met. The grey bars illustrate the maximum error, as estimated by Monte Carlo simulations.

Observations from the two airborne systems ALADINA and BELUGA are presented in Fig. 15. To provide a broader overview of the meteorological and aerosol conditions during the measurement day, data from the first vertical ascending profiles of each flight of both systems are presented. The potential temperature θ derived from ALADINA measurements (see Fig. 15b) indicates a stably stratified ABL throughout the day, with θ increasing with altitude in all profiles. The strongest vertical gradients occur in the lowest few hundred meters, with a pronounced stable layer near the surface and a transition layer around 250–400 m characterised by a smaller vertical gradient. Above this layer, θ continues to increase more gradually with altitude, while profiles after 17:00 UTC show additional enhanced gradients at higher altitudes, indicating further stable layering aloft in the latter part of the measurement period. Vertical profiles of N_6 from ALADINA (see Fig. 15a) show substantial variability between the individual profiles. The first profile at 09:15 UTC demonstrates elevated N_6 reaching 1,900 cm^{-3} observed at altitudes below 200 m a.s.l., indicating an enhanced aerosol layer near the surface. This layer coincides with pronounced stable stratification in the potential temperature profile, suggesting limited vertical exchange in the lower ABL in the morning. In contrast, the profiles at 15:15 UTC and 16:08 UTC show a more vertically homogeneous distribution of N_6 of

https://doi.org/10.5194/essd-2026-411
Preprint. Discussion started: 28 July 2026

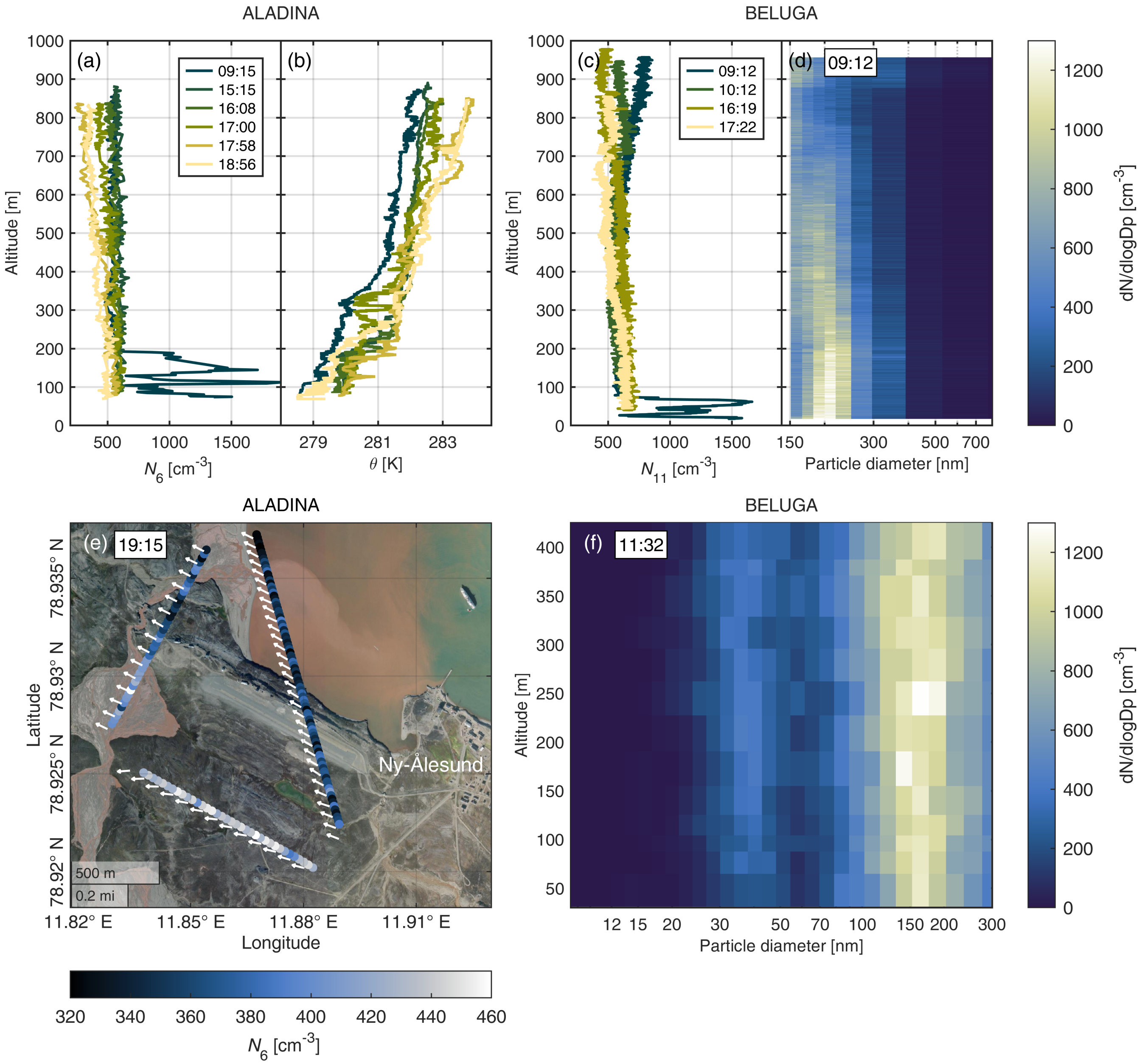

Figure 15. Observations from the two airborne systems ALADINA and BELUGA on 3 June 2024. Given times indicate the start of a respective vertical profile or a horizontal pattern in UTC. Panels (a) and (b) show N_6 and potential temperature θ, respectively, from the first vertical profile during all ALADINA flights performed on 3 June 2024. Panel (c) shows N_{11} from all ascending BELUGA profiles obtained with the CAMP platform on 3 June 2024, while panel (d) presents an exemplary ascending BELUGA profile of the $PNSD$ measured by the POPS on CAMP at 09:12 UTC. Panel (e) shows N_6 and arrows indicating a 3 s rolling median of DD during an exemplary horizontal ALADINA pattern flown at constant altitude of 430 m a.s.l. at 19:15 UTC. Panel (f) presents an exemplary ascending BELUGA profile of the $PNSD$ derived from the mSEMS at 11:32 UTC. Map data source panel (e): Earthstar Geographics.

approximately 500 cm^{-3} increasing to 600 cm^{-3}. After 17:00 UTC, profiles of N_6 show a gradual decrease in the overall concentration level below 500 cm^{-3}, while remaining relatively homogeneous within the lowest 300 m. The observed decrease in particle concentration may be consistent with deposition processes, as indicated by the negative particle flux between 13:00 UTC and 17:00 UTC measured from the gradient system. Above 300 m, N_6 decreases with altitude reaching a minimum of about 250 cm^{-3}. This vertical structure coincides with stronger gradients in θ, suggesting reduced vertical mixing. Vertical profiles of N_{11} from BELUGA (see Fig. 15c) generally align with the observations from ALADINA, showing a similar layer of increased particle concentration at 09:12 UTC at low altitudes below 100 m. The reduced vertical extent of this pronounced aerosol layer compared to ALADINA, where enhanced concentrations were observed up to about 200 m a.s.l., may be related to the different measurement locations of the two systems with different terrain elevation and local variability in the ABL. Furthermore, profiles of N_{11} after 10 UTC similarly demonstrate a more vertically homogeneous distribution. During the first two BELUGA profiles, N_{11} increases with altitude, reaching values of up to approximately 800 cm^{-3}, whereas after 16:00 UTC, it decreases with altitude, reaching a minimum below 500 cm^{-3}.

The vertical profile of $PNSD$ at 09:12 UTC (see Fig. 15d), derived from the CAMP platform of BELUGA, demonstrates a predominant aerosol particle size in the accumulation mode between 150 nm and 300 nm and an absence of particles larger than 400 nm. This observation is complemented by an additional vertical profile of $PNSD$ at 11:32 UTC (see Fig. 15f), derived from the mSEMS platform of BELUGA. This profile demonstrates an additional aerosol particle mode in the Aitken mode between 30 nm and 50 nm, and the absence of smaller particles below 30 nm. Consequently, observations of N_6 from ALADINA and N_{11} from BELUGA (see Fig. 15a,c) show similar particle concentrations, despite the varying lower cut-off sizes. Finally, the horizontal distribution of N_6 is presented in Fig. 15e, showing an exemplary horizontal ALADINA flight pattern at constant altitude of 430 m a.s.l. at 19:15 UTC. The horizontal pattern indicates a higher aerosol particle concentration above land, reaching values above 450 cm^{-3} and a lower concentration around 350 cm^{-3} to 400 cm^{-3} above the Kongsfjord in the transect by crossing the coastline. The wind direction along the horizontal flight path (see Fig. 15e) was predominantly homogeneous, with DD around 120°. A moderate alteration in wind direction in the southern part of the pattern indicates local variations, potentially influenced by the orography surrounding Zeppelin Mountain, which may have contributed to the observed horizontal variability in N_6.

Overall, the observations indicate that the spatial distribution of aerosol particles on 3 June 2024 was influenced by the combined effects of changing advection, surface exchange and stable stratification. The transition of wind direction to East, together with increasing wind speed, enhanced short-wave irradiance, positive sensible heat flux and net particle deposition, is consistent with the observed vertical and horizontal variability in aerosol properties and the stable stratification of the ABL observed by ALADINA and BELUGA.

5 Conclusions

This publication presents a combined data set of airborne and surface-based observations obtained during a field campaign in Ny-Ålesund in spring 2024. The three measurement systems provide complementary information on aerosol and meteorologi-

https://doi.org/10.5194/essd-2026-411
Preprint. Discussion started: 28 July 2026

cal conditions in the lower Arctic atmosphere. The UAS ALADINA resolves the spatial variability of aerosol particle number concentration and thermodynamic properties through repeated vertical profiles and horizontal flight patterns, while the tethered balloon system BELUGA extends the vertical profiling capability and provides additional aerosol size distribution. The surface flux-gradient system adds continuous near-surface measurements and enables estimates of sensible heat and particle fluxes. The case study on 3 June 2024 demonstrates how the combined observations can be used to relate aerosol variability to boundary-layer structure, meteorological conditions and surface exchange processes. The combined use of UAS, tethered balloon and surface flux measurements therefore provides a valuable observational basis for investigating aerosol processes and their interaction with atmospheric dynamics in the Arctic boundary layer.

6 Data availability

The ALADINA data are available on PANGAEA at https://doi.org/10.1594/PANGAEA.988207 (Schuchard et al., 2026). In addition to the data presented in Table 2, the final data set includes the aircraft's position (latitude, longitude, and altitude a.s.l. referenced to WGS84) and attitude information (roll, pitch, heading). BELUGA data are published on PANGAEA at https://doi.org/10.1594/PANGAEA.988353 (Kellermann et al., 2026), including data from the TMP and the aerosol platforms CAMP and mSEMS. Data of the surface flux gradient system are available at https://doi.org/10.1594/PANGAEA.984519 on PANGAEA (Mathes et al., 2025b).

Video supplement. A short video illustrates the operation of the UAS ALADINA from take-off to landing using different camera perspectives. Most sequences were recorded during measurement days in June 2024, after the onset of snow melt. The video has been submitted to the German National Library of Science and Technology (TIB) and the DOI will be provided in the final manuscript.

Author contributions. The contact author MS wrote the main text and contributed to the figures. MS, KB, LB, TC, MK, TM, JM, CP, AS, BW, BH participated in the field campaign. MS, KB, MK, TM, CP, AH, AS, HS were responsible for data post-processing. BW, AL acquired funding for this project and supported the data analyses. MK, TM, AS, BW provided text and contributed to the figures. RK and CP conducted the calibration of aerosol sensors at TROPOS. All authors provided feedback on results, and revised the manuscript.

Competing interests. The authors declare that they have no conflict of interest.

Acknowledgements. This work was funded by the German Research Foundation (Deutsche Forschungsgemeinschaft, DFG) project "Aerosol variability and interaction with ambient conditions based on small-scale vertical and horizontal distribution of Arctic measurements (AIDA)" under grant 519822612. The field campaign in Ny-Ålesund was supported by the AWIPEV Research Base (AWIPEV_0031; RiS ID 12274).

https://doi.org/10.5194/essd-2026-411
Preprint. Discussion started: 28 July 2026

The Polar and Arctic Atmosphere Research Group at the University of Helsinki, including Matthew Boyer, Zoé Brasseur, Lauriane Quéléver, Nina Sarnela, Mikko Sipilä, Roseline Thakur, Cecilia Righi and Aarni Vaittinen, as well as the Institute of Polar Sciences at the National Research Council (Italy), including Stefania Gilardoni and Mauro Mazzola, provided important ground-based measurements of the aerosol particle size distribution to support the data post-processing. The authors would like to thank Marion Maturilli, Christoph Ritter, Radovan Krejci, Dominic Heslin-Rees, Matthew Boyer, the entire AWIPEV team and the crew of the Kings Bay AS for their support during the field campaign.

https://doi.org/10.5194/essd-2026-411
Preprint. Discussion started: 28 July 2026

References

Albrecht, B. A.: Aerosols, cloud microphysics, and fractional cloudiness, Science (New York, N.Y.), 245, 1227–1230, https://doi.org/10.1126/science.245.4923.1227, 1989.

Altstädter, B., Platis, A., Wehner, B., Scholtz, A., Wildmann, N., Hermann, M., Käthner, R., Baars, H., Bange, J., and Lampert, A.: ALADINA – an unmanned research aircraft for observing vertical and horizontal distributions of ultrafine particles within the atmospheric boundary layer, Atmospheric Measurement Techniques, 8, 1627–1639, https://doi.org/10.5194/amt-8-1627-2015, 2015.

Arrhenius, S.: Über die Reaktionsgeschwindigkeit bei der Inversion von Rohrzucker durch Säuren, Zeitschrift für Physikalische Chemie, 4U, 226–248, https://doi.org/10.1515/zpch-1889-0416, 1889.

Bärfuss, K. B., Schmithüsen, H., and Lampert, A.: Drone-based meteorological observations up to the tropopause – a concept study, Atmospheric Measurement Techniques, 16, 3739–3765, https://doi.org/10.5194/amt-16-3739-2023, 2023.

Beck, L. J., Sarnela, N., Junninen, H., Hoppe, C. J. M., Garmash, O., Bianchi, F., Riva, M., Rose, C., Peräkylä, O., Wimmer, D., Kausiala, O., Jokinen, T., Ahonen, L., Mikkilä, J., Hakala, J., He, X.-C., Kontkanen, J., Wolf, K. K. E., Cappelletti, D., Mazzola, M., Traversi, R., Petroselli, C., Viola, A. P., Vitale, V., Lange, R., Massling, A., Nøjgaard, J. K., Krejci, R., Karlsson, L., Zieger, P., Jang, S., Lee, K., Vakkari, V., Lampilahti, J., Thakur, R. C., Leino, K., Kangasluoma, J., Duplissy, E.-M., Siivola, E., Marbouti, M., Tham, Y. J., Saiz-Lopez, A., Petäjä, T., Ehn, M., Worsnop, D. R., Skov, H., Kulmala, M., Kerminen, V.-M., and Sipilä, M.: Differing Mechanisms of New Particle Formation at Two Arctic Sites, Geophysical Research Letters, 48, e2020GL091 334, https://doi.org/10.1029/2020GL091334, 2021.

Beine, H. J., Argentini, S., Maurizi, A., Mastrantonio, G., and Viola, A.: The local wind field at Ny-Ålesund and the Zeppelin mountain at Svalbard, Meteorology and Atmospheric Physics, 78, 107–113, https://doi.org/10.1007/s007030170009, 2001.

Boike, J., Juszak, I., Lange, S., Chadburn, S., Burke, E., Overduin, P. P., Roth, K., Ippisch, O., Bornemann, N., Stern, L., Gouttevin, I., Hauber, E., and Westermann, S.: A 20-year record (1998–2017) of permafrost, active layer and meteorological conditions at a high Arctic permafrost research site (Bayelva, Spitsbergen), Earth System Science Data, 10, 355–390, https://doi.org/10.5194/essd-10-355-2018, 2018.

Boike, J., Grünberg, I., Miesner, F., Bornemann, N., and Cable, W. L.: Continuous measurements in soil and air at the permafrost long-term observatory at the Bayelva station near Ny-Ålesund (2018 et seq), https://doi.org/10.1594/PANGAEA.948951, 2022.

Boyer, M.: 2024 NAIS at Gruvebadet, https://doi.org/10.71761/55624457-D6BA-4E30-9765-2205B62BF4AD, 2025.

Bretschneider, L., Schlerf, A., Baum, A., Bohlius, H., Buchholz, M., Düsing, S., Ebert, V., Erraji, H., Frost, P., Käthner, R., Krüger, T., Lange, A. C., Langner, M., Nowak, A., Pätzold, F., Rüdiger, J., Saturno, J., Scholz, H., Schuldt, T., Seldschopf, R., Sobotta, A., Tillmann, R., Wehner, B., Wesolek, C., Wolf, K., and Lampert, A.: MesSBAR—Multicopter and Instrumentation for Air Quality Research, Atmosphere, 13, https://doi.org/10.3390/atmos13040629, 2022.

Browse, J., Carslaw, K. S., Mann, G. W., Birch, C. E., Arnold, S. R., and Leck, C.: The complex response of Arctic aerosol to sea-ice retreat, Atmospheric Chemistry and Physics, 14, 7543–7557, https://doi.org/10.5194/acp-14-7543-2014, 2014.

Businger, J. A., Wyngaard, J. C., Izumi, Y., and Bradley, E. F.: Flux-Profile Relationships in the Atmospheric Surface Layer, Journal of the Atmospheric Sciences, 28, 181–189, https://doi.org/10.1175/1520-0469(1971)028<0181:FPRITA>2.0.CO;2, 1971.

Bärfuss, K., Pätzold, F., Altstädter, B., Kathe, E., Nowak, S., Bretschneider, L., Bestmann, U., and Lampert, A.: New Setup of the UAS ALADINA for Measuring Boundary Layer Properties, Atmospheric Particles and Solar Radiation, Atmosphere, 9, https://doi.org/10.3390/atmos9010028, 2018.

https://doi.org/10.5194/essd-2026-411
Preprint. Discussion started: 28 July 2026

Charlson, R. J., Langner, J., Rodhe, H., Leovy, C. B., and Warren, S. G.: Perturbation of the northern hemisphere radiative balance by backscattering from anthropogenic sulfate aerosols*, Tellus A: Dynamic Meteorology and Oceanography, 43, 152, https://doi.org/10.3402/tellusa.v43i4.11944, 1991.

Chen, C., Dubovik, O., Schuster, G. L., Fuertes, D., Meijer, Y., Landgraf, J., Karol, Y., and Li, Z.: Characterization of temporal and spatial variability of aerosols from ground-based climatology: towards evaluation of satellite mission requirements, Journal of Quantitative Spectroscopy and Radiative Transfer, 268, 107 627, https://doi.org/10.1016/j.jqsrt.2021.107627, 2021.

Chung, P.-C. and Feldl, N.: Sea Ice Loss, Water Vapor Increases, and Their Interactions with Atmospheric Energy Transport in Driving Seasonal Polar Amplification, Journal of Climate, 37, 2713 – 2725, https://doi.org/10.1175/JCLI-D-23-0219.1, 2024.

Crameri, F.: Scientific colour maps, https://doi.org/10.5281/zenodo.8409685, 2023.

Dai, A., Luo, D., Song, M., and Liu, J.: Arctic amplification is caused by sea-ice loss under increasing CO2, Nature Communications, 10, 121, https://doi.org/10.1038/s41467-018-07954-9, 2019.

Dall´Osto, M., Beddows, D. C. S., Tunved, P., Krejci, R., Ström, J., Hansson, H.-C., Yoon, Y. J., Park, K.-T., Becagli, S., Udisti, R., Onasch, T., O´Dowd, C. D., Simó, R., and Harrison, R. M.: Arctic sea ice melt leads to atmospheric new particle formation, Scientific Reports, 7, 3318, https://doi.org/10.1038/s41598-017-03328-1, 2017.

Dall´Osto, M., Geels, C., Beddows, D. C. S., Boertmann, D., Lange, R., Nøjgaard, J. K., Harrison, R. M., Simo, R., Skov, H., and Massling, A.: Regions of open water and melting sea ice drive new particle formation in North East Greenland, Scientific Reports, 8, 6109, https://doi.org/10.1038/s41598-018-24426-8, 2018.

Dall'Osto, M., Park, J., Kim, J.-H., Kang, S.-H., Park, K., Beddows, D., Harrison, R. M., and Yoon, Y.: Arctic ship-based evidence of new particle formation events in the Chukchi and East Siberian Seas, Atmospheric Environment, 223, 117 232, https://doi.org/10.1016/j.atmosenv.2019.117232, 2020.

Dorff, H., Siebert, H., Navale, K., Ehrlich, A., Müller, J., Schäfer, M., Wu, F., and Wendisch, M.: Tethered balloon-borne measurements to characterise the evolution of the Arctic atmospheric boundary layer at Station Nord, Earth System Science Data Discussions, 2025, 1–28, https://doi.org/10.5194/essd-2025-651, 2025.

Duplessis, P., Karlsson, L., Baccarini, A., Wheeler, M., Leaitch, W. R., Svenningsson, B., Leck, C., Schmale, J., Zieger, P., and Chang, R. Y.-W.: Highly Hygroscopic Aerosols Facilitate Summer and Early-Autumn Cloud Formation at Extremely Low Concentrations Over the Central Arctic Ocean, Journal of Geophysical Research: Atmospheres, 129, e2023JD039 159, https://doi.org/10.1029/2023JD039159, 2024.

Ebell, K., Nomokonova, T., Maturilli, M., and Ritter, C.: Radiative effect of clouds at Ny–Ålesund, Svalbard, as inferred from ground-based remote sensing observations, J. Appl. Meteor. Climatol., 59, 3–22, 2020.

Egerer, U., Gottschalk, M., Siebert, H., Ehrlich, A., and Wendisch, M.: The new BELUGA setup for collocated turbulence and radiation measurements using a tethered balloon: first applications in the cloudy Arctic boundary layer, Atmospheric Measurement Techniques, 12, 4019–4038, https://doi.org/10.5194/amt-12-4019-2019, 2019.

Felden, J., Möller, L., Schindler, U., Huber, R., Schumacher, S., Koppe, R., Diepenbroek, M., and Glöckner, F. O.: PANGAEA - Data Publisher for Earth & Environmental Science, Scientific data, 10, 347, https://doi.org/10.1038/s41597-023-02269-x, 2023.

Foken, T. and Mauder, M.: Micrometeorology, Springer Atmospheric Sciences, Springer International Publishing, Cham, ISBN 978-3-031-47525-2 978-3-031-47526-9, https://doi.org/10.1007/978-3-031-47526-9, 2024.

Frey, M. M., Norris, S. J., Brooks, I. M., Anderson, P. S., Nishimura, K., Yang, X., Jones, A. E., Nerentorp Mastromonaco, M. G., Jones, D. H., and Wolff, E. W.: First direct observation of sea salt aerosol production from blowing snow above sea ice, Atmospheric Chemistry and Physics, 20, 2549–2578, https://doi.org/10.5194/acp-20-2549-2020, 2020.

Gao, R. S., Telg, H., McLaughlin, R. J., Ciciora, S. J., Watts, L. A., Richardson, M. S., Schwarz, J. P., Perring, A. E., Thornberry, T. D., Rollins, A. W., Markovic, M. Z., Bates, T. S., Johnson, J. E., and Fahey, D. W.: A light-weight, high-sensitivity particle spectrometer for PM2.5 aerosol measurements, Aerosol Science and Technology, 50, 88–99, https://doi.org/10.1080/02786826.2015.1131809, 2016.

Goosse, H., Kay, J. E., Armour, K. C., Bodas-Salcedo, A., Chepfer, H., Docquier, D., Jonko, A., Kushner, P. J., Lecomte, O., Massonnet, F., Park, H.-S., Pithan, F., Svensson, G., and Vancoppenolle, M.: Quantifying climate feedbacks in polar regions, Nature Communications, 9, 1919, https://doi.org/10.1038/s41467-018-04173-0, 2018.

Gormley, P. G. and Kennedy, M.: Diffusion from a Stream Flowing through a Cylindrical Tube, Proc. Royal Irish Academy, pp. 163–169, 1949.

Graßl, S., Ritter, C., and Schulz, A.: The Nature of the Ny-Ålesund Wind Field Analysed by High-Resolution Windlidar Data, Remote Sensing, 14, https://doi.org/10.3390/rs14153771, 2022.

Harm-Altstädter, B., Bärfuss, K., Bretschneider, L., Schön, M., Bange, J., Käthner, R., Krejci, R., Mazzola, M., Park, K., Pätzold, F., Peuker, A., Traversi, R., Wehner, B., and Lampert, A.: Spatial distribution and variability of boundary layer aerosol particles observed in Ny-Ålesund during late spring in 2018, Aerosol Research, 1, 39–64, https://doi.org/10.5194/ar-1-39-2023, 2023.

Harm-Altstädter, B., Voß, A., Aust, S., Bärfuss, K., Bretschneider, L., Merkel, M., Pätzold, F., Schlerf, A., Weinhold, K., Wiedensohler, A., Winkler, U., and Lampert, A.: First study using a fixed-wing drone for systematic measurements of aerosol vertical distribution close to a civil airport, Frontiers in Environmental Science, Volume 12 - 2024, https://doi.org/10.3389/fenvs.2024.1376980, 2024.

Held, A., Orsini, D. A., Vaattovaara, P., Tjernström, M., and Leck, C.: Near-surface profiles of aerosol number concentration and temperature over the Arctic Ocean, Atmospheric Measurement Techniques, 4, 1603–1616, https://doi.org/10.5194/amt-4-1603-2011, 2011.

Holton, J. R. and Hakim, G. J.: An introduction to dynamic meteorology, Academic Press, Amsterdam, fifth edition edn., ISBN 9780123848666, 2013.

Huang, Y., Huang, H., and Shakirova, A.: The Nonlinear Radiative Feedback Effects in the Arctic Warming, Frontiers in Earth Science, Volume 9 - 2021, https://doi.org/10.3389/feart.2021.693779, 2021.

Igel, A. L., Ekman, A. M. L., Leck, C., Tjernström, M., Savre, J., and Sedlar, J.: The free troposphere as a potential source of arctic boundary layer aerosol particles, Geophysical Research Letters, 44, 7053–7060, https://doi.org/10.1002/2017GL073808, 2017.

Kellermann, M., Conrath, T., Käthner, R., Mathes, T., Müller, J., Pilz, C., Wehner, B., Schuchard, M., and Siebert, H.: Tethered balloon-borne measurements of meteorological and aerosol microphysical properties during the Arctic melt season 2024 [dataset bundled publication], PANGAEA, https://doi.org/10.1594/PANGAEA.988353, 2026.

Kim, Y.-H., Min, S.-K., Gillett, N. P., Notz, D., and Malinina, E.: Observationally-constrained projections of an ice-free Arctic even under a low emission scenario, Nature Communications, 14, 3139, https://doi.org/10.1038/s41467-023-38511-8, 2023.

Kulkarni, P., Baron, P. A., and Willeke, K., eds.: Aerosol Measurement: Principles, Techniques, and Applications, Wiley, J, New York, NY, 3., auflage edn., ISBN 9780470387412, 2011.

Laidler, K. J.: The development of the Arrhenius equation, Journal of Chemical Education, 61, 494, https://doi.org/10.1021/ed061p494, 1984.

Lampert, A., Altstädter, B., Bärfuss, K., Bretschneider, L., Sandgaard, J., Michaelis, J., Lobitz, L., Asmussen, M., Damm, E., Käthner, R., Krüger, T., Lüpkes, C., Nowak, S., Peuker, A., Rausch, T., Reiser, F., Scholtz, A., Sotomayor Zakharov, D., Gaus, D., Bansmer, S.,

https://doi.org/10.5194/essd-2026-411
Preprint. Discussion started: 28 July 2026

Wehner, B., and Pätzold, F.: Unmanned Aerial Systems for Investigating the Polar Atmospheric Boundary Layer—Technical Challenges and Examples of Applications, Atmosphere, 11, https://doi.org/10.3390/atmos11040416, 2020.

Leck, C., Norman, M., Bigg, E. K., and Hillamo, R.: Chemical composition and sources of the high Arctic aerosol relevant for cloud formation, Journal of Geophysical Research: Atmospheres, 107, AAC 1–1–AAC 1–17, https://doi.org/10.1029/2001JD001463, 2002.

Lee, H., Lee, K., Lunder, C. R., Krejci, R., Aas, W., Park, J., Park, K.-T., Lee, B. Y., Yoon, Y. J., and Park, K.: Atmospheric new particle formation characteristics in the Arctic as measured at Mount Zeppelin, Svalbard, from 2016 to 2018, Atmospheric Chemistry and Physics, 20, 13 425–13 441, https://doi.org/10.5194/acp-20-13425-2020, 2020.

Lenschow, D.: The measurement of air velocity and temperature using the NCAR Buffalo Aircraft Measuring System, https://doi.org/10.5065/D6C8277W, 1972.

Lupi, A., Busetto, M., Becagli, S., Giardi, F., Lanconelli, C., Mazzola, M., Udisti, R., Hansson, H.-C., Henning, T., Petkov, B., Ström, J., Krejci, R., Tunved, P., Viola, A. P., and Vitale, V.: Multi-seasonal ultrafine aerosol particle number concentration measurements at the Gruvebadet observatory, Ny-Ålesund, Svalbard Islands, Rendiconti Lincei, 27, 59–71, https://doi.org/10.1007/s12210-016-0532-8, 2016.

Mathes, T., Guy, H., Prytherch, J., Kojoj, J., Brooks, I., Murto, S., Zieger, P., Wehner, B., Tjernström, M., and Held, A.: Particle flux–gradient relationships in the high Arctic: emission and deposition patterns across three surface types, Atmospheric Chemistry and Physics, 25, 8455–8474, https://doi.org/10.5194/acp-25-8455-2025, 2025a.

Mathes, T., Pilz, C., Otterbach, L.-M., Wehner, B., and Held, A.: Particle flux-gradient relationships for the expedition AIDA, Ny Alesund, 2024 [dataset bundled publication], PANGAEA, https://doi.org/10.1594/PANGAEA.984519, 2025b.

Matsui, H. and Liu, M.: Substantial Uncertainties in Arctic Aerosol Simulations by Microphysical Processes Within the Global Climate-Aerosol Model CAM-ATRAS, Journal of Geophysical Research: Atmospheres, 127, e2022JD036 943, https://doi.org/10.1029/2022JD036943, 2022.

Maturilli, M.: Continuous meteorological observations at station Ny-Ålesund (2011-08 et seq), https://doi.org/10.1594/PANGAEA.914979, 2020a.

Maturilli, M.: Basic and other measurements of radiation at station Ny-Ålesund (2006-05 et seq), https://doi.org/10.1594/PANGAEA.914927, 2020b.

Maturilli, M.: Ceilometer cloud base height from station Ny-Ålesund (2017-08 et seq), https://doi.org/10.1594/PANGAEA.942331, 2022.

Maturilli, M. and Ebell, K.: Twenty-five years of cloud base height measurements by ceilometer in Ny-Ålesund, Svalbard, Earth System Science Data, 10, 1451–1456, https://doi.org/10.5194/essd-10-1451-2018, 2018.

Maturilli, M., Herber, A., and König-Langlo, G.: Climatology and time series of surface meteorology in Ny-Ålesund, Svalbard, Earth System Science Data, 5, 155–163, https://doi.org/10.5194/essd-5-155-2013, 2013.

Mauritsen, T., Sedlar, J., Tjernström, M., Leck, C., Martin, M., Shupe, M., Sjogren, S., Sierau, B., Persson, P. O. G., Brooks, I. M., and Swietlicki, E.: An Arctic CCN-limited cloud-aerosol regime, Atmos. Chem. Phys., 11, 165–173, https://doi.org/10.5194/acp-11-165-2011, 2011.

Mungall, E. L., Abbatt, J. P. D., Wentzell, J. J. B., Lee, A. K. Y., Thomas, J. L., Blais, M., Gosselin, M., Miller, L. A., Papakyriakou, T., Willis, M. D., and Liggio, J.: Microlayer source of oxygenated volatile organic compounds in the summertime marine Arctic boundary layer, Proceedings of the National Academy of Sciences, 114, 6203–6208, https://doi.org/10.1073/pnas.1620571114, 2017.

Orellana, M. V., Matrai, P. A., Leck, C., Rauschenberg, C. D., Lee, A. M., and Coz, E.: Marine microgels as a source of cloud condensation nuclei in the high Arctic, Proceedings of the National Academy of Sciences, 108, 13 612–13 617, https://doi.org/10.1073/pnas.1102457108, 2011.

https://doi.org/10.5194/essd-2026-411
Preprint. Discussion started: 28 July 2026

Pernov, J. B., Beddows, D., Thomas, D. C., Dall´Osto, M., Harrison, R. M., Schmale, J., Skov, H., and Massling, A.: Increased aerosol concentrations in the High Arctic attributable to changing atmospheric transport patterns, npj Climate and Atmospheric Science, 5, 62, https://doi.org/10.1038/s41612-022-00286-y, 2022.

Pilz, C., Düsing, S., Wehner, B., Müller, T., Siebert, H., Voigtländer, J., and Lonardi, M.: CAMP: an instrumented platform for balloon-borne aerosol particle studies in the lower atmosphere, Atmospheric Measurement Techniques, 15, 6889–6905, https://doi.org/10.5194/amt-15-6889-2022, publisher: Copernicus GmbH, 2022.

Pilz, C., Lonardi, M., Egerer, U., Siebert, H., Ehrlich, A., Heymsfield, A. J., Schmitt, C. G., Shupe, M. D., Wehner, B., and Wendisch, M.: Profile observations of the Arctic atmospheric boundary layer with the BELUGA tethered balloon during MOSAiC, Scientific Data 2023 10:1, 10, 1–12, https://doi.org/10.1038/s41597-023-02423-5, 2023.

Pithan, F. and Mauritsen, T.: Arctic amplification dominated by temperature feedbacks in contemporary climate models, Nature Geoscience, 7, 181–184, https://doi.org/10.1038/ngeo2071, 2014.

Platis, A., Altstädter, B., Wehner, B., Wildmann, N., Lampert, A., Hermann, M., Birmili, W., and Bange, J.: An Observational Case Study on the Influence of Atmospheric Boundary-Layer Dynamics on New Particle Formation, Boundary-Layer Meteorology, 158, 67–92, https://doi.org/10.1007/s10546-015-0084-y, 2016.

Platt, S. M., Hov, Ø., Berg, T., Breivik, K., Eckhardt, S., Eleftheriadis, K., Evangeliou, N., Fiebig, M., Fisher, R., Hansen, G., Hansson, H.-C., Heintzenberg, J., Hermansen, O., Heslin-Rees, D., Holmén, K., Hudson, S., Kallenborn, R., Krejci, R., Krognes, T., Larssen, S., Lowry, D., Lund Myhre, C., Lunder, C., Nisbet, E., Nizzetto, P. B., Park, K.-T., Pedersen, C. A., Aspmo Pfaffhuber, K., Röckmann, T., Schmidbauer, N., Solberg, S., Stohl, A., Ström, J., Svendby, T., Tunved, P., Tørnkvist, K., van der Veen, C., Vratolis, S., Yoon, Y. J., Yttri, K. E., Zieger, P., Aas, W., and Tørseth, K.: Atmospheric composition in the European Arctic and 30 years of the Zeppelin Observatory, Ny-Ålesund, Atmospheric Chemistry and Physics, 22, 3321–3369, https://doi.org/10.5194/acp-22-3321-2022, 2022.

Price, R., Baccarini, A., Schmale, J., Zieger, P., Brooks, I. M., Field, P., and Carslaw, K. S.: Late summer transition from a free-tropospheric to boundary layer source of Aitken mode aerosol in the high Arctic, Atmospheric Chemistry and Physics, 23, 2927–2961, https://doi.org/10.5194/acp-23-2927-2023, 2023.

Prohasky, D. and Watkins, S.: Low Cost Hot-element Anemometry Verses the TFI Cobra, in: 19th Australasian Fluid Mechanics Conference, 2014.

Rantanen, M., Karpechko, A. Y., Lipponen, A., Nordling, K., Hyvärinen, O., Ruosteenoja, K., Vihma, T., and Laaksonen, A.: The Arctic has warmed nearly four times faster than the globe since 1979, Communications Earth Environment, 3, 168, https://doi.org/10.1038/s43247-022-00498-3, 2022.

Schmale, J., Zieger, P., and Ekman, A. M. L.: Aerosols in current and future Arctic climate, Nature Climate Change, 11, 95–105, https://doi.org/10.1038/s41558-020-00969-5, 2021.

Schuchard, M., Bärfuss, K., Bretschneider, L., Käthner, R., Lampert, A., Pilz, C., Schlerf, A., and Harm-Altstädter, B.: Airborne measurements of Arctic aerosol and meteorological parameters using the UAV ALADINA in Ny-Ålesund during melting season in May/June 2024 [dataset publication series], PANGAEA, https://doi.org/10.1594/PANGAEA.988207, 2026.

Schön, M., Suomi, I., Altstädter, B., van Kesteren, B., zum Berge, K., Platis, A., Wehner, B., Lampert, A., and Bange, J.: Case studies of the wind field around Ny-Ålesund, Svalbard, using unmanned aircraft, Polar Research, 41, https://doi.org/10.33265/polar.v41.7884, 2022.

Shupe, M. D. and Intrieri, J. M.: Cloud Radiative Forcing of the Arctic Surface: The Influence of Cloud Properties, Surface Albedo, and Solar Zenith Angle, Journal of Climate, 17, 616 – 628, https://doi.org/10.1175/1520-0442(2004)017<0616:CRFOTA>2.0.CO;2, 2004.

https://doi.org/10.5194/essd-2026-411
Preprint. Discussion started: 28 July 2026

Standish, E. M.: JPL Planetary and Lunar Ephemerides, DE405/LE405, Tech. Rep. IOM 312.F-98-048, Jet Propulsion Laboratory, California Institute of Technology, Pasadena, CA, https://ssd.jpl.nasa.gov/planets/eph_export.html, 1998.

Stohl, A.: Characteristics of atmospheric transport into the Arctic troposphere, Journal of Geophysical Research: Atmospheres, 111, https://doi.org/10.1029/2005JD006888, 2006.

Tuch, T., Weinhold, K., Merkel, M., Nowak, A., Klein, T., Quincey, P., Stolzenburg, M., and Wiedensohler, A.: Dependence of CPC cut-off diameter on particle morphology and other factors, Aerosol Science and Technology, 50, 331–338, https://doi.org/10.1080/02786826.2016.1152351, 2016.

Tunved, P., Ström, J., and Krejci, R.: Arctic aerosol life cycle: linking aerosol size distributions observed between 2000 and 2010 with air mass transport and precipitation at Zeppelin station, Ny-Ålesund, Svalbard, Atmospheric Chemistry and Physics, 13, 3643–3660, https://doi.org/10.5194/acp-13-3643-2013, 2013.

Twomey, S.: The Influence of Pollution on the Shortwave Albedo of Clouds, Journal of the Atmospheric Sciences, 34, 1149–1152, https://doi.org/10.1175/1520-0469(1977)034<1149:TIOPOT>2.0.CO;2, 1977.

Vancoppenolle, M., Meiners, K. M., Michel, C., Bopp, L., Brabant, F., Carnat, G., Delille, B., Lannuzel, D., Madec, G., Moreau, S., Tison, J.-L., and van der Merwe, P.: Role of sea ice in global biogeochemical cycles: emerging views and challenges, Quaternary Science Reviews, 79, 207–230, https://doi.org/10.1016/j.quascirev.2013.04.011, sea Ice in the Paleoclimate System: the Challenge of Reconstructing Sea Ice from Proxies, 2013.

Wang, Y., Jiang, J. H., Su, H., Choi, Y.-S., Huang, L., Guo, J., and Yung, Y. L.: Elucidating the Role of Anthropogenic Aerosols in Arctic Sea Ice Variations, Journal of Climate, 31, 99 – 114, https://doi.org/10.1175/JCLI-D-17-0287.1, 2018.

Watanabe, T. K. and Pfeiffer, M.: A simple Monte Carlo approach to estimate the uncertainties of SST and δ18Osw inferred from coral proxies, Geochemistry, Geophysics, Geosystems, 23, e2021GC009 813, https://doi.org/10.1029/2021GC009813, 2022.

Wendisch, M., Brückner, M., Crewell, S., Ehrlich, A., Notholt, J., Lüpkes, C., Macke, A., Burrows, J. P., Rinke, A., Quaas, J., Maturilli, M., Schemann, V., Shupe, M. D., Akansu, E. F., Barrientos-Velasco, C., Bärfuss, K., Blechschmidt, A.-M., Block, K., Bougoudis, I., Bozem, H., Böckmann, C., Bracher, A., Bresson, H., Bretschneider, L., Buschmann, M., Chechin, D. G., Chylik, J., Dahlke, S., Deneke, H., Dethloff, K., Donth, T., Dorn, W., Dupuy, R., Ebell, K., Egerer, U., Engelmann, R., Eppers, O., Gerdes, R., Gierens, R., Gorodetskaya, I. V., Gottschalk, M., Griesche, H., Gryanik, V. M., Handorf, D., Harm-Altstädter, B., Hartmann, J., Hartmann, M., Heinold, B., Herber, A., Herrmann, H., Heygster, G., Höschel, I., Hofmann, Z., Hölemann, J., Hünerbein, A., Jafariserajehlou, S., Jäkel, E., Jacobi, C., Janout, M., Jansen, F., Jourdan, O., Jurányi, Z., Kalesse-Los, H., Kanzow, T., Käthner, R., Kliesch, L. L., Klingebiel, M., Knudsen, E. M., Kovács, T., Körtke, W., Krampe, D., Kretzschmar, J., Kreyling, D., Kulla, B., Kunkel, D., Lampert, A., Lauer, M., Lelli, L., von Lerber, A., Linke, O., Löhnert, U., Lonardi, M., Losa, S. N., Losch, M., Maahn, M., Mech, M., Mei, L., Mertes, S., Metzner, E., Mewes, D., Michaelis, J., Mioche, G., Moser, M., Nakoudi, K., Neggers, R., Neuber, R., Nomokonova, T., Oelker, J., Papakonstantinou-Presvelou, I., Pätzold, F., Pefanis, V., Pohl, C., van Pinxteren, M., Radovan, A., Rhein, M., Rex, M., Richter, A., Risse, N., Ritter, C., Rostosky, P., Rozanov, V. V., Donoso, E. R., Saavedra Garfias, P., Salzmann, M., Schacht, J., Schäfer, M., Schneider, J., Schnierstein, N., Seifert, P., Seo, S., Siebert, H., Soppa, M. A., Spreen, G., Stachlewska, I. S., Stapf, J., Stratmann, F., Tegen, I., Viceto, C., Voigt, C., Vountas, M., Walbröl, A., Walter, M., Wehner, B., Wex, H., Willmes, S., Zanatta, M., and Zeppenfeld, S.: Atmospheric and Surface Processes, and Feedback Mechanisms Determining Arctic Amplification: A Review of First Results and Prospects of the (AC)3 Project, Bulletin of the American Meteorological Society, 104, E208–E242, https://doi.org/10.1175/bams-d-21-0218.1, 2023.

https://doi.org/10.5194/essd-2026-411
Preprint. Discussion started: 28 July 2026

Open Access Earth System Science Data Discussions

Wiedensohler, A., Wiesner, A., Weinhold, K., Birmili, W., Hermann, M., Merkel, M., Müller, T., Pfeifer, S., Schmidt, A., Tuch, T., Velarde, F., Quincey, P., Seeger, S., and Nowak, A.: Mobility particle size spectrometers: Calibration procedures and measurement uncertainties, Aerosol Science and Technology, 52, 146–164, https://doi.org/10.1080/02786826.2017.1387229, 2018.

Wieringa, J.: A revaluation of the Kansas mast influence on measurements of stress and cup anemometer overspeeding, Boundary layer meteorology, 18, 411–430, https://doi.org/10.1007/BF00119497, 1980.

Zitoun, R., Marcinek, S., Hatje, V., Sander, S. G., Völker, C., Sarin, M., and Omanović, D.: Climate change driven effects on transport, fate and biogeochemistry of trace element contaminants in coastal marine ecosystems, Communications Earth & Environment, 5, 560, 2024.